Influence of capillary end effects on steady-state relative permeability estimates from direct pore-scale simulations

Gaël Raymond Guédon,[1, a)] Jeffrey De'Haven Hyman,[2] Fabio Inzoli,[1] Monica Riva,[3, 4] and Alberto Guadagnini[3, 4]

[1)] *Dipartimento di Energia, Politecnico di Milano, Via Lambruschini 4a, 20156 Milano, Italy*

[2)] *Computational Earth Science Group (EES-16), Earth and Environmental Sciences Division, Los Alamos National Laboratory, Los Alamos, NM 87545, USA*

[3)] *Dipartimento di Ingegneria Civile e Ambientale, Politecnico di Milano, Piazza L. Da Vinci 32, 20133 Milano, Italy*

[4)] *Department of Hydrology and Atmospheric Sciences, University of Arizona, Tucson, AZ 85721, USA*

(Dated: 27 November 2017)

We investigate and characterize the influence of capillary end effects on steady-state relative permeabilities obtained in pore-scale numerical simulations of two-phase flows. Our study is motivated by the observation that capillary end effects documented in two-phase laboratory-scale experiments can significantly influence permeability estimates. While numerical simulations of two-phase flows in reconstructed pore-spaces are increasingly employed to characterize relative permeabilities, a phenomenon which is akin to capillary end effects can also arise in such analyses due to the constraints applied at the boundaries of the computational domain. We profile the relative strength of these capillary end effects on the calculation of steady-state relative permeabilities obtained within randomly generated porous micro-structures using a finite volume-based two-phase flow solver. We suggest a procedure to estimate the extent of the regions influenced by these capillary end effects, which in turn allows for the alleviation of bias in the estimation of relative permeabilities.

PACS numbers: 47.56.+r,47.61.Jd, 91.60.Np,47.11.Df

[a)] gaelraymond.guedon@polimi.it

I. INTRODUCTION

Relative permeability quantifies the rate of displacement of a fluid phase under an applied pressure gradient in the presence of multiple fluid phases in a porous medium. It is a fundamental parameter for a variety of applications in the field of energy and environmental engineering, including assessment of the impact of conventional and unconventional hydrocarbon extraction on groundwater bodies, as well as CO_2 storage in subsurface systems.[1–3] Data of relative permeability versus fluid saturation are typically obtained from laboratory experiments of multi-phase flow in rock plugs extracted from reservoirs. Due to the experimental set-up, capillary end effects are commonly observed at the outlet as a result of the capillary jump generated by the discontinuity in the solid matrix at the interface between the rock sample and the outlet.[4,5] Capillary pressure in the core plug is related to the porous structure and saturation history, while capillary pressure vanishes at the outlet. This discontinuity produces a large pressure gradient in the non-wetting fluid phase that influences the saturation and pressure distribution across the length of the sample and typically yields an accumulation of the wetting phase near the outlet. Consequently, the values of relative permeability and phases saturation inferred from an experiment can be markedly influenced by the experimental set-up employed.[6–9]

Two prevailing experimental techniques for the determination of relative permeabilities in laboratory samples are: *(a)* the unsteady-state and *(b)* the steady-state methods. In the former, a displacement process (e.g., drainage or imbibition) is induced and pressure drop and (average) phase saturation are continuously monitored across the porous medium sample. Relative permeabilities are indirectly evaluated, typically using the Johnson, Bossler and Naumann (JBN) method[10] or variants thereof. All fluids are simultaneously injected in a steady-state experiment.[9,11] A given total fluid flow rate is typically imposed and diverse fractional flow rates are considered. The fluids are generally circulated in a closed loop system and total pressure drop across the sample, flow rates and fluid saturations are continuously measured. Steady-state conditions are reached when the fractional flow rates at the outlet of the porous medium are equal to that at the inlet and the total pressure drop has stabilized. A key advantage of the steady-state method is the simpler data elaboration required to estimate relative permeabilities. The method is also less prone to capillary end effects as higher flow rates can be used to mitigate these without altering the estimates of relative permeability curves.[12] However, these experiments are much more time-consuming than their unsteady-state counterpart.

With the increasing availability of high resolution tomographic images of complex pore-spaces within rock core plugs and the development of numerical simulation techniques that yield accurate pore-scale distributions of state variables governing multi-phase relative permeabilities, an increasing number of studies has been devoted to the assessment of relative permeabilities through direct numerical simulations of multi-phase flow settings. Modeling multi-phase flow in porous media is a challenging task, as it concerns forces acting at diverse scales in the flow domain. Currently available numerical approaches are based on *(a)* direct numerical simulation (DNS), including grid- and particle-based methods, where equations describing processes governing fluid displacement are directly solved in the three-dimensional complex geometry defined by the tomography images and *(b)* pore network models (PNM) where the complex geometry of the rock is simplified through a collection of pores and channels (throats) to which a set of simplified equations and rules is applied. Pore-network models are nowadays in an advanced state of development and extensive reviews can be found in the literature.[13–18] Otherwise, the development of direct numerical simulation techniques for multi-phase flows is relatively recent and diverse approaches are still being developed for this purpose, cf., Ref. 19 for a recent review. The main advantage of DNS simulations over PNM is the absence of simplified flow processes and consequently the potential for results with increased accuracy. Eulerian grid-based finite volume solvers are considered as a preferred computational fluid dynamics (CFD) approach for solving the Navier-Stokes equations and has also shown promising capabilities for the simulation of two-phase flow in explicit pore-spaces associated with porous/fractured rocks.[19–25] Reviews of the most common numerical methods employed in this context can be found in Refs. 19–21, 26–31.

Similar to experiments, constraints, e.g., boundary conditions, applied in the numerical simulations can lead to the emergence of end effects that influence computed values of relative permeability. The consequences of these end effects on estimates of pore-scale relative permeability in numerical simulations have not yet been completely investigated. The work by Ramstad *et al.*[32] constitutes one of the scarce studies simulating two-phase flows in porous media implementing and comparing both the steady- and unsteady-state methods. While the presence of end effects are mentioned in these works, detailed analyses on the matter are not offered. In this context, we offer a study of the influence of such phenomena on the estimates of relative permeabilities as a function of pore-space observables (such as porosity, specific surface area and pore size distribution) as well as experimental operating parameters (such as capillary number and fluid viscosity ratio).

Binary representations of real porous media obtained by segmenting high resolution images of porous micro-structures imaged using X-ray tomography, or related techniques, are commonly used in pore-scale simulations.[33–36] These samples are often too small to guarantee the attainment of stable spatial statistics of functionals describing the topology and morphology of the porous system (as embedded, e.g., in the Minkowski functionals, including, e.g., porosity, specific surface area, or mean curvature) and do not allow performing a systematic analysis of the effects of target processes. As such, the resulting flow simulations can be limited in scope, with reference to the characterization of boundary effects on relative permeability estimates. Additionally, the availability of samples and the costs of imaging can limit the number of realizations that can be taken directly from images[37] so that robust statistical analyses can hardly be performed.

Here, we model a two-phase fluid flow setting by mimicking steady-state protocols employed for relative permeability laboratory-scale experiments to assess the strength of the boundary condition effects, i.e., capillary end effects, on the resulting relative permeability estimates. Co-injection of a wetting (i.e., water) and a non-wetting (i.e., oil) fluid phase is simulated within synthetic three-dimensional pore-spaces using a finite volume-based solver. The use of synthetic pore-spaces that are isotropic, statistically-stationary, and large enough to produce stable statistics in terms of both geometric and physical observables alleviates the aforementioned issues associated with using binary representations of actual rock samples. We consider three porous micro-structures with varying pore sizes and the same values of porosity ($\phi = 0.48$), and develop a framework for the quantitative assessment of the magnitude of these boundary effects. As a result, using this computational setup we propose and illustrate a method for the evaluation of relative permeabilities that excludes the regions of the pore-space affected by boundary conditions. In this sense, our study contributes to the ongoing development of procedures for the determination of pore-scale relative permeabilities.

The work is structured as follows. First, we describe the procedure adopted for the generation of the porous micro-structures and characterize their geometric observables (Sec-

II A). Next, we present the numerical methods used to resolve two-phase flow within the pore-spaces (Section II B). We discuss our results in Section III A, from which we derive a methodology to identify capillary end effects in Section III B. The influence of capillary end effects on relative permeability values is assessed and discussed in Section III C. We end with conclusions and provide guidelines for an appropriate evaluation of relative permeabilities in porous micro-structures in Section IV.

II. METHODS

A. Generation of pore-spaces

The method we use for pore-space generation was introduced in Smolarkiewicz and Winter.[38] The method is structured according to the three steps described in the following.

1. Each node on a three-dimensional regular grid with uniform spacing h is assigned an independent identically distributed random value, $u(\mathbf{x})$ ($\mathbf{x}$, being the vector of grid node coordinates), sampled from a continuous uniform distribution on the closed interval $[0, 1]$. Here, we set $h = 5$ μm.

2. This random field is convolved with a symmetric Gaussian kernel, $k(\mathbf{x}, \beta)$, with an intrinsic length scale β, to generate the isotropic correlated random topography,

$$T(\mathbf{x}) = \int_{\mathbb{R}^3} k(\mathbf{x} - \mathbf{y}, \beta) u(\mathbf{y}) d\mathbf{y} \tag{1}$$

   The value of β determines the correlation length in the topography.

3. After T is created, a level threshold, $\gamma \in [0, 1]$, is applied to T to map values onto an indicator function, I, where $I(\mathbf{x}) = 1$ in the pore voxels and $I(\mathbf{x}) = 0$ otherwise, i.e.,

$$I(\mathbf{x}) = \begin{cases} 0 & , \text{ if } T(\mathbf{x}) \geq \gamma \\ 1 & , \text{ if } T(\mathbf{x}) < \gamma \end{cases} \tag{2}$$

   If the value of $T(\mathbf{x})$ is greater than γ, then $\mathbf{x}$ is considered to be in the solid matrix, otherwise $\mathbf{x}$ is in the void space. Intuitively, as γ increases so does the volume of the void space in the porous medium.

TABLE I: Generation parameters and geometric observables of the samples investigated.

Sample	β	γ	ϕ	$\bar{r}_{\text{pores}}$ [m]	N_{pores}	s	r	L_z/λ
A	0.015 h	0.50	0.48	$8.48{\cdot}10^{-6}$	1681	0.25	4 h	341.33
B	0.030 h	0.50	0.48	$1.84{\cdot}10^{-5}$	428	0.25	9 h	151.70
C	0.045 h	0.50	0.48	$2.02\cdot10^{-5}$	335	0.25	10 h	136.53

Two elements to note are that values in the topography $T(\mathrm{x})$ are normally distributed, a consequence of the central limit theorem, and the indicator function $I(\mathbf{x})$ is stationary and ergodic.[39]

Hyman and Winter[39] provided a rigorous theoretical investigation of the method complemented by an extensive set of detailed numerical simulations to characterize the way the generation parameters govern pore-space geometric observables, e.g., porosity and specific surface area. Hyman *et al.*[40] investigated scaling behavior of geometric observables of such generated samples and found that these display symptoms of statistical scaling that have also been observed in real millimeter scale rock samples.[41] Virtual pore-spaces generated using this method have been combined with (single-phase fluid) flow and transport simulations to investigate the influence of porosity on transport properties,[42] porosity and mean hydraulic radius of the pore-space on absolute permeability,[43] pore-wall geometry and network topology on local mixing of dissolved chemicals,[44] and pore-size distributions on in-pore fluid velocity distributions.[45]

In this study we generate three porous media samples with dimensions of $(L_x = 64h) \times (L_y = 64h) \times (L_z = 512h)$ and total volume of 2.097×10^{-12} m^3, hereafter termed as setting A, B, and C, respectively denoting systems with increasing average pore size. Generation parameters and geometric observables of the samples are listed in Table I. The average pore radii and number of pores are computed using the maximal ball algorithm described in Ref. 46. A three-dimensional overview of the sample geometries is provided in Figure 1. Note that wider kernels (higher values of β) lead to pore-spaces with fewer and wider pores than those generated with smaller values of β.

We quantify the degree of the spatial correlation of the void space by calculating the variogram $\gamma(h^*)$ of the indicator function I.[47] The variogram is a function that describes the

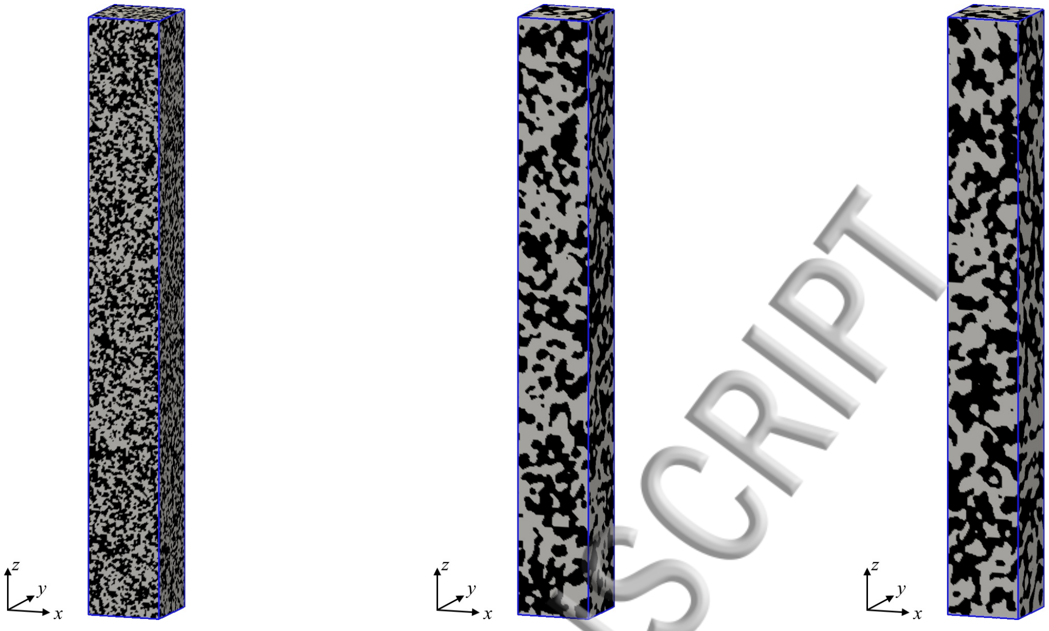

(a) Sample A (b) Sample B (c) Sample C

FIG. 1: Isometric view of the porous medium analyzed (black is pore-space; gray is solid phase) for a) sample A, b) sample B, and c) sample C.

degree of spatial dependence of a random field by measuring the variance of the difference between values in the field at two locations $\mathbf{x}_i$ and $\mathbf{x}_j$. If the field is stationary, as is the one we consider here, then the variogram $\gamma(h^*)$ tends asymptotically to a sill s whose theoretical value is equal to $\phi(1-\phi)$, the variance of I,[47] that does not depend on β. We begin by computing the empirical variogram

$$\hat{\gamma}(h^*) = \frac{1}{2N(h^*)} \sum_{(i,j)\in N(h^*)} |I_i - I_j|^2 \tag{3}$$

where $N(h^*)$ denotes the number of pairs of observations i and j such that $|\mathbf{x}_i - \mathbf{x}_j| = h^*$. We employ the following spherical model to characterize (3),

$$\gamma(h^*) = \begin{cases} s\left(\frac{3h^*}{2r} - \frac{h^{*3}}{2r^3}\right) & : 0 < h^* \leq r \\ s & : h^* > r \end{cases} \tag{4}$$

where r is the (isotropic) range. An integral measure of the spatial correlation is provided by the integral scale of I, λ, defined as

$$\lambda = \frac{1}{s}\int_0^\infty [s - \gamma(h^*)]dh^* \tag{5}$$

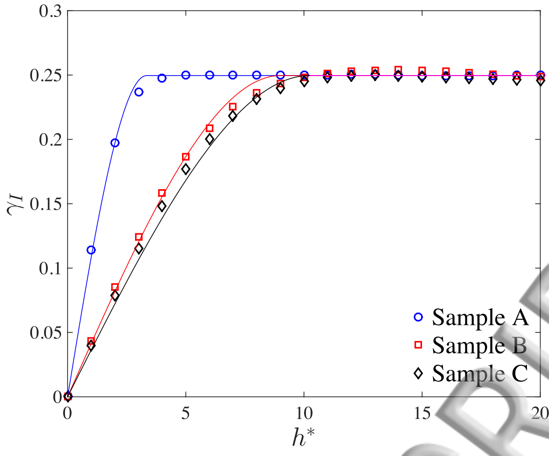

FIG. 2: Empirical (symbols) and calibrated (continuous curves) variograms of the indicator function, I, for the three samples analyzed.

Combining (4) and (5) reveals that $\lambda = 3r/8$. Values of the model parameters in (4) are estimated by minimizing the ℓ^2 norm between (3) and (4) over r and are listed in Table I. The latter also lists the ratios L_z/λ, which measures the number of integral length scales in each sample along the vertical direction. Empirical and calibrated variograms are depicted in Figure 2.

B. Two-phase flow solver

Direct numerical simulation of two-phase flow within the generated three-dimensional pore-spaces is performed using a finite volume method. The governing equations for each phase are the Navier-Stokes equations for incompressible, isothermal and Newtonian fluids. In order to track the position of the interface, the set of equations is supplemented by the volume fraction transport equation of one of the two phases. In the following, we use the one-fluid formulation[48–50] governed by:

$$\frac{\partial \rho}{\partial t} + \nabla \cdot (\rho \mathbf{u}) = 0 \tag{6}$$

$$\frac{\partial \rho \mathbf{u}}{\partial t} + \nabla \cdot (\rho \mathbf{u}\mathbf{u}) = -\nabla p + \nabla \cdot \left[\mu \left(\nabla \mathbf{u} + \nabla \mathbf{u}^\top\right)\right] + \sigma \kappa \mathbf{n} \delta_{\text{int}} \tag{7}$$

$$\frac{\partial \alpha}{\partial t} + \nabla \cdot (\alpha \mathbf{u}) = 0 \tag{8}$$

AIP Publishing

Here, t is time, $\mathbf{u}$ denotes the velocity vector, p is pressure, α is the local volume fraction of one of the two phases, ρ is density, μ is dynamic viscosity, σ is surface tension coefficient, δ_{int} is a Dirac delta function that is non-null at the location of the interface between the two fluids, and $\kappa = \nabla \cdot \mathbf{n}$ is the mean curvature of the interface, $\mathbf{n} = \frac{\nabla\alpha}{|\nabla\alpha|}$ being the vector normal to the interface. Local values of density and dynamic viscosity are calculated as weighted averages of the density and dynamic viscosity of the fluid phases:

$$\rho = \alpha\rho_1 + (1-\alpha)\,\rho_2 \tag{9}$$

$$\mu = \alpha\mu_1 + (1-\alpha)\,\mu_2 \tag{10}$$

subscript $i (i = 1, 2)$ denoting fluid phase i, α being the local volume fraction of fluid phase $i = 1$. The surface tension, (see the last term in Eq. (7)), is approximated using the Continuum Surface Force (CSF) model of Brackbill *et al.*[51]:

$$\sigma\kappa\mathbf{n}\delta_{\text{int}} \approx \sigma\kappa\nabla\alpha \tag{11}$$

The OpenFOAM® open-source CFD library, release 2.4.0, is used to solve the target system of equations through the built-in solver `multiphaseInterFoam`.[52] Standard numerical schemes are used in this software to solve the continuity and momentum equations, while the transport equations of the volume fractions are modified to include an extra, artificial compression term, as described in Refs. 53 and 54. This term is added to compensate numerical diffusion that is typically associated with the transport of a sharp function, such as the volume fraction. In order to preserve boundedness and conservativeness, the MULES (Multidimensional Universal Limiter with Explicit Solution) solver is also used to correct the volume fraction fluxes.[52] Second order upwind interpolation schemes are implemented to calculate the convective terms in the governing equations. Time discretization is performed using a first order Euler implicit scheme and the time step size is adapted such that the Courant number is below 0.8.

The geometrical discretization of the pore-space is performed such that each voxel of the three-dimensional binary geometry data is converted into a cubic cell. This results in a staircase-like boundary, i.e., a first order approximation of the solid geometry. Advantages associated with this representation include a higher stability, due to the absence of explicit non-orthogonal corrections, faster computation, and automatic mesh generation capabilities. To achieve such discretization efficiently, an ad-hoc mesh generator was developed. In

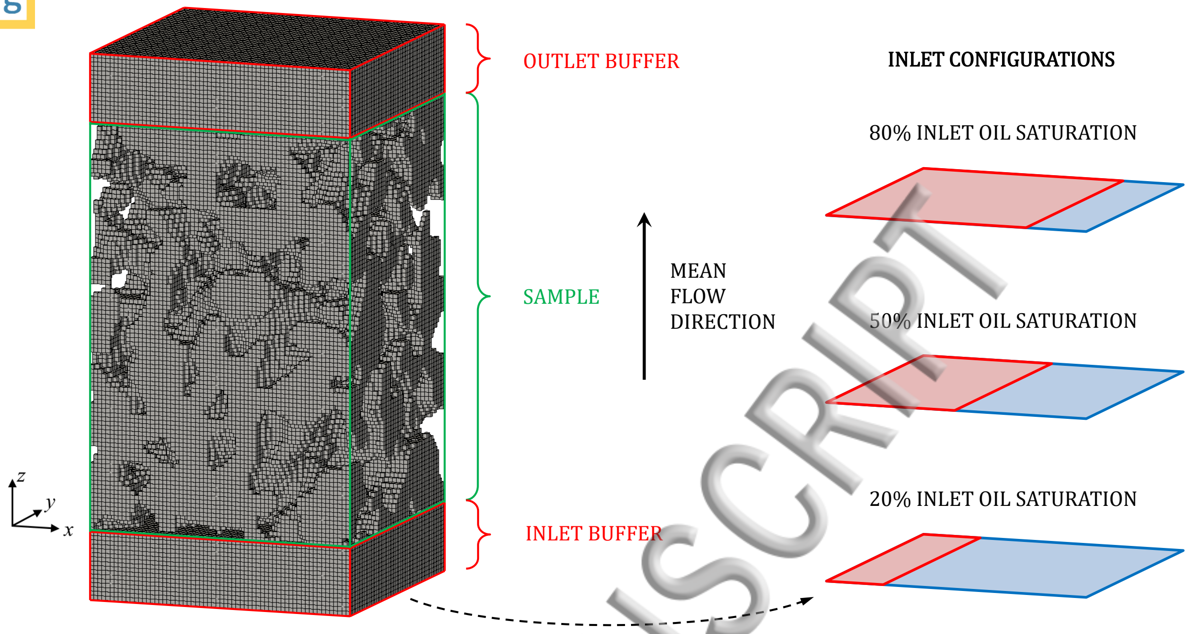

FIG. 3: Example of meshed void space with the added inlet and outlet buffer regions, and illustration of the three inlet configurations used in the simulations.

addition to the discretization of the pore-space geometry, empty buffer regions of size $16h$ are inserted at the inlet and outlet of the sample, as depicted in Figure 3. These regions are used to mimic a real laboratory experimental setup, as discussed in the following sections. Preliminary sensitivity studies showed that the quantities analyzed in Section III do not depend significantly on the size of the buffer regions (details not shown). Note that in the following the vertical evolution of the quantities of interest are showed by setting the coordinate $z = 0$ at the base of the porous sample (i.e., results within the buffer area are not reported).

The simultaneous flow of a wetting (water) and a non-wetting (oil) phase is considered. As initial conditions, the pore-space is fully saturated with water at rest. Free-slip conditions for the velocity and homogeneous Neumann conditions for the pressure and volume fraction are imposed along the lateral boundaries of the system. Given velocity and volume fraction are assigned at the bottom (inlet), pressure being fixed at the top (outlet) of the sample. No-slip conditions are implemented on the internal walls, with a contact angle (measured through the water phase) of 30°, corresponding to water-wet conditions. Three cases of fixed

TABLE II: Parameters of the simulations.

Parameter	Value
Density ratio, ρ_o/ρ_w	1
Viscosity ratio, μ_o/μ_w	2
Surface tension coefficient, σ [N/m]	10^{-4}
Water Reynolds number, $\mathrm{Re}_w = \rho_w \overline{U} \bar{d}_{\mathrm{pores}}/\phi\mu_w$	$\approx 6 \times 10^{-3}$
Oil Reynolds number, $\mathrm{Re}_o = \rho_o \overline{U} \bar{d}_{\mathrm{pores}}/\phi\mu_o$	$\approx 3 \times 10^{-3}$
Water capillary number, $\mathrm{Ca}_w = \mu_w \overline{U}/\sigma$	10^{-3}
Oil capillary number, $\mathrm{Ca}_o = \mu_o \overline{U}/\sigma$	2×10^{-3}

oil volume fraction at the inlet (equal to 20%, 50% or 80%, as illustrated in Figure 3) are considered.

The inlet velocity, $\overline{U}$, and the fluid properties are set according to the parameters listed in Table II. Due to the inlet configuration, $\overline{U}$ coincides with Darcy velocity. We start by setting the fluid densities and viscosities and by defining the inlet velocity such that the Reynolds number (Re) satisfies the Stokes flow condition (i.e., Re $\ll$ 1). We define the Reynolds number, Re, through the average fluid velocity in the porous medium, $\overline{U}/\phi$, and the average pore diameter, $\bar{d}_{\mathrm{pores}} = 2\bar{r}_{\mathrm{pores}}$. We then adjust the surface tension coefficient of the fluids to attain a given value for the capillary number, Ca. In this study, we set $\mathrm{Ca} = \mathcal{O}(10^{-3})$, which yields a relatively low value for the surface tension coefficient, σ. Our choice for Ca is motivated by requirements associated with *(a)* computational time, that increases significantly as Ca decreases;[20,21] and *(b)* the relative strength of capillary end effects that may be too high at lower values of Ca, thus inhibiting the possibility to observe regions unaffected by end effects on the pore-spaces considered. Note that similar values of Ca were implemented in other studies.[21,28] From a physical standpoint, the value of σ we consider is characteristic of oil and water flow with surfactants.[55]

We define the time required to complete one pore volume displacement as:

$$T_{\mathrm{pore}} = \frac{V_{\mathrm{pore}}}{\overline{U} A_{\mathrm{inlet}}} \tag{12}$$

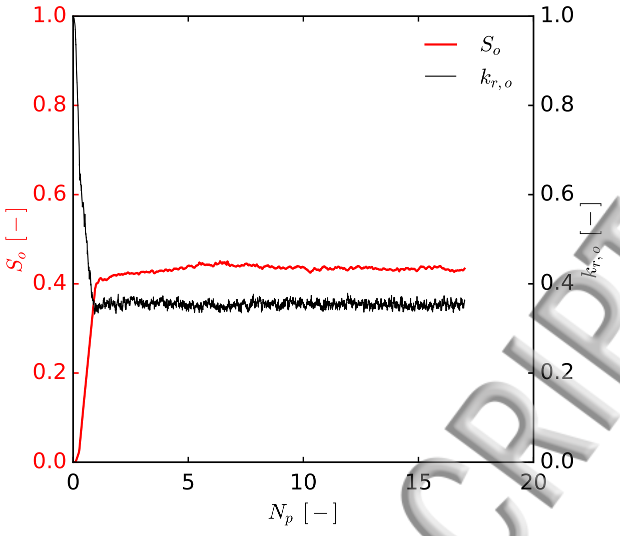

FIG. 4: Volume-averaged oil saturation and oil relative permeability versus injected pore volumes for sample B and 50% of inlet oil saturation.

V_{pore} and A_{inlet} respectively being the volume of the pore-space and the inlet section area. The simulated two-phase flow exhibits an initial transient behavior during which the oil phase percolates through the medium. This is then followed by a periodic regime. The numerical simulations have been implemented according to the following two steps: *(a)* an initial run is performed for $5T_{\mathrm{pore}}$ to reach the above mentioned periodic conditions; *(b)* a second run is then completed for $(N_p - 5)T_{\mathrm{pore}}$. Simulation results are then processed via the evaluation of time and section-averaged quantities, as detailed in Appendix A. The number of pore volumes (i.e., N_p) required to obtain significant temporal statistics of the variables of interest has been determined through a sensitivity study. We find that relative variations in the time-averaged quantities of interest (e.g., oil saturation and pressure) are smaller than 2% increasing $(N_p - 5)$ from 4 to 12. Figure 4 illustrates the time evolution of the volume-averaged oil saturation and oil relative permeability as a function of N_p for sample B and considering 50% inlet oil saturation. Only results obtained with $(N_p - 5) = 4$ are reported in Section III.

TABLE III: Absolute permeabilities (expressed in Darcy) as a function of l_z/h.

Sample	32	64	96	128	160	192	228	256	512
A	1.88	1.73	1.64	1.61	1.62	1.61	1.63	1.64	1.62
B	11.87	11.39	9.28	9.31	9.22	8.80	8.47	8.44	8.96
C	17.99	11.21	10.47	10.55	10.38	10.99	10.94	11.12	10.41

III. RESULTS AND DISCUSSION

To assess the strength of capillary end effects on all of the time and section-averaged quantities of interest nine subsamples of increasing length l_z along the z-direction were extracted from the three samples A, B and C, starting from $z = 0$, while keeping $L_x = 64h$ and $L_y = 64h$. Varying the length of the computational domain enables us to assess the sensitivity of the results to end effects, as smaller domains are more prone to be influenced by such phenomena. In the following we report the results obtained with $l_z = i \times 32h$ (with $i = 1...8$), $512h$ for each pore size characteristic (sample A, B or C) and the three oil inlet saturations reported in Figure 3, for a total of 81 simulations. The naming convention for each case simulated is: *Sample*–l_z–$S_{o,\text{inlet}}$. *Sample* will refer to the sample A, B or C, and $S_{o,\text{inlet}}$ is the inlet oil saturation.

For the sake of completeness, values of absolute permeabilities of each subsample evaluated through single-phase fluid flow simulations are listed in Table III.

A. Local distribution of pressures and oil saturation

The behavior of the fluid phases is determined by the local arrangement of the pore-space, saturations, and pressures across the medium, such as those illustrated in Figure 5 for sample A–$192h$–50%. The key elements consistently observed in the simulations and characterizing the behavior of our target quantities are described in the following.

a. Porosity The section-averaged porosity profile (Figure 5a) displays oscillations around the mean value ($\phi = 0.48$) which are indicative of statistical stationarity and homogeneity of the sample. The amplitude of these oscillations, which is a proxy for the assessment of the spatial variability of the porosity, tends to increase with the magnitude of the integral scale, λ, of the indicator function, I (not shown). A similar behavior is observed for all samples.

b. Oil saturation The time and section-averaged (as defined in Appendix A) oil saturation profile (Figure 5b) allows evidencing the relative distribution of oil in the void space as function of the distance from the inlet. Such a saturation profile is characterized by large values near the inlet (denoting accumulation of the non-wetting phase) and low values in proximity of the outlet (corresponding to accumulation of the wetting phase). A similar behavior has been observed in laboratory experiments.[4,5,7,9] Kyte and Rapoport[7] describe the inlet end effects in water-wet media as "a result of spontaneous, localized imbibition". As water approaches the inlet face, only a relatively small area will be interrogated and water will spontaneously imbibe into the pore-space to continue entering the medium solely in a localized area. This feature in turn results in an increased oil saturation near the inlet region. Osoba *et al.*[6] depicts outlet end effects in water-wet media as a consequence of the action of capillary forces in the pore-space which tend to retain the wetting phase at the outflow end. This would then result in "an accumulation of the wetting phase, so that the saturation of that phase at the outflow boundary is maintained at a higher level than throughout the remainder of the core".

c. Pressure Distributions Time and section-averaged pressure profiles in the oil and water phase (Figure 5c) display sensibly linear trends in the bulk of the medium. Deviations from these linear trends in the proximity of the inlet and outlet regions are evidences of end effects. Pressure drops are observed near the entrance for the wetting phase (water), suggesting that the velocity of the wetting phase strongly increases in this region. This feature is consistent with the description of inlet end effects by Kyte and Rapoport,[7] who state that a "spontaneous imbitition" occurs at the inlet. Otherwise, pronounced pressure drops are noticed in the non-wetting phase (oil) near the exit of the system. Indeed, as the oil approaches the outlet, it experiences an increased resistance from the water phase that is retained by the porous structure. As such, the oil is allowed to exit the medium only through a localized region corresponding to the one with the lowest oil flow resistance, resulting in higher oil velocities and consequently in higher pressure drops.

d. Capillary pressure Capillary pressure (Figure 5d) is an indicator of the average difference of pressure between the non-wetting and wetting phases. It is governed by the curvature of the interfaces between the phases. In a porous medium, the structure of the solid phase and the size of the pores play an important role in determining these interfaces and hence capillary pressure. Our simulations show that capillary pressure tends to vanish at the inlet and outlet boundaries. This behavior is the result of the empty buffer regions used to impose inlet and outlet boundary conditions: *(a)* the outlet boundary condition provides a constraint of constant pressure for both phases (i.e., zero capillary pressure); while *(b)* the vertical flow imposed at the inlet boundary for both oil and water phases forces the capillary pressure to be zero since the interface between the two phases is planar at locations corresponding to the inlet boundary face. With reference to conditions that are typically achieved in laboratory settings, one can note that these types of discontinuities in the solid matrix are naturally present at the inlet and outlet ends of the rock sample, which is inserted in a closed-loop hydraulic circuit. These discontinuities yield a build up of capillary pressure at the system entrance, as the phases progressively enter the medium, and to a vanishing capillary pressure at the outflow end.

In summary, the distributions of pressures and saturations in the bulk of the pore-space display average trends (linear for pressures and mostly uniform for saturations) over which oscillations due to local heterogeneity are superimposed. These oscillations are less pronounced as the magnitude of the integral scale, λ, of the indicator function, I, decreases. Otherwise, the distributions of pressures and saturations in the proximity of the inlet and outlet of the domain display moderate to strong deviations from the above evidenced undisturbed (or bulk) trends. These deviations are likely to be caused by capillary end effects due to the discontinuity of the solid matrix and boundary conditions. Hence, it is critical to identify the extent and relative strength of these effects to obtain appropriate estimates of relative permeabilities to relate to volume-averaged fluid saturations across the sample.

B. Identification of capillary end effects

As illustrated previously, capillary end effects give rise to modifications of the distribution and behavior of the water and oil phases in the medium investigated in proximity of the inlet and outlet regions. We quantify the extent of these disturbed regions by comparing the distributions of oil saturation and water and oil pressures in the medium against undisturbed bulk trends.

AIP Publishing

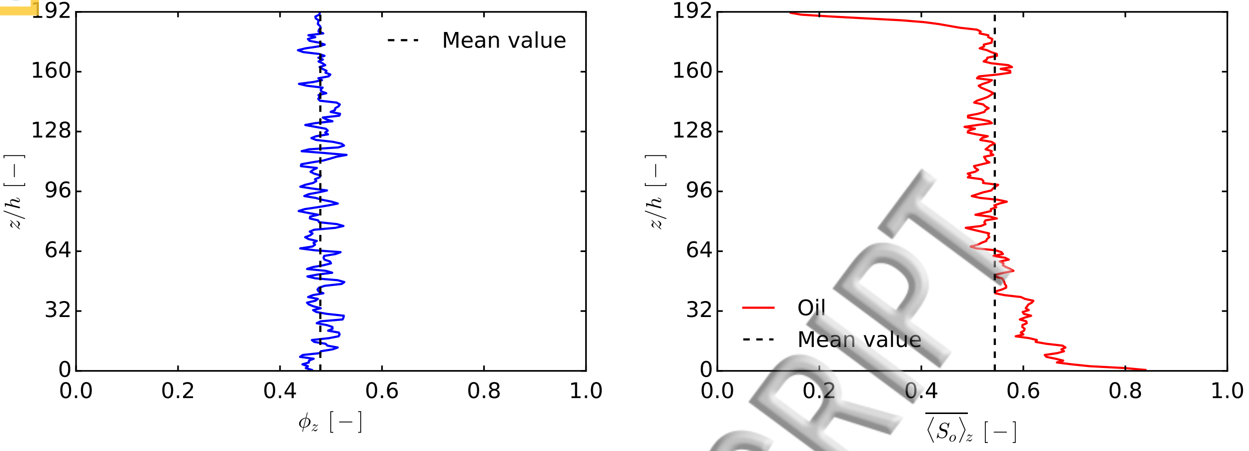

(a) Porosity (b) Oil saturation

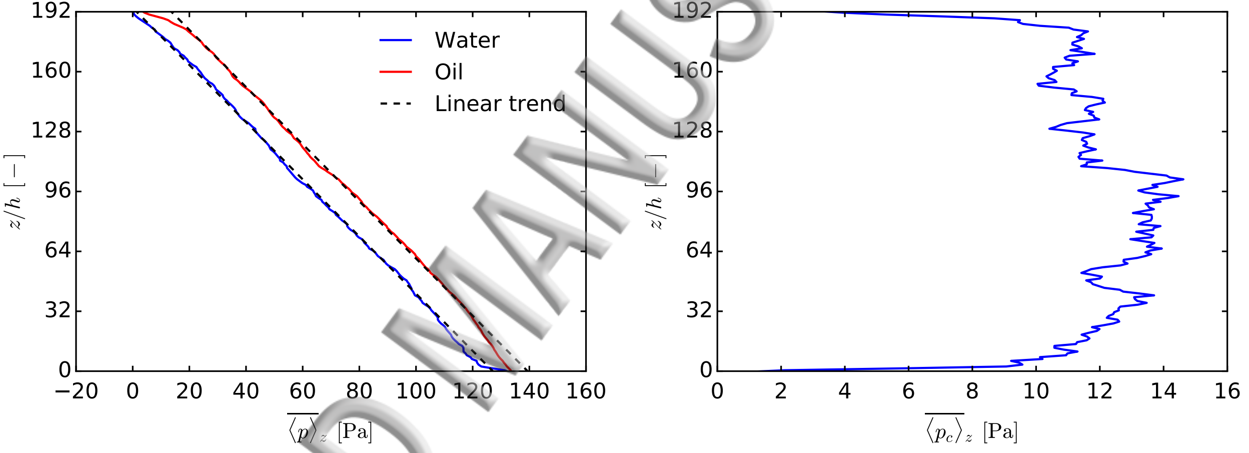

(c) Water and oil pressures (d) Capillary pressure

FIG. 5: Distribution of a) section-averaged porosity, b) time and section-averaged oil saturation, c) time and section-averaged water and oil pressures, and d) time and section-averaged capillary pressure, for case A–192h–50%.

The distribution of section-averaged pressure along the mean flow direction in an infinite homogeneous medium is linear. Identification of the region where the undisturbed trends of water and oil pressures take place is here obtained by best fit of such pressure distributions to linear functions. The latter are constrained to display the same slope for both fluid phases, because time- and section-averaged capillary pressure is constant throughout an infinite macroscopically homogeneous medium. Such a model for undisturbed pressure trends is applicable here because of the generation method implemented that ensures stationarity of the pore-space. Oscillations in time- and section-averaged capillary pressure are noticed due to local inhomogeneities and finite section area of the samples analyzed. Note that such oscillations would disappear as the section area tends to infinity and the time- and section-averaged capillary pressure would be constant throughout the region unaffected by end effects. An example of such an analysis is depicted in Figure 5c. Significant deviations from these linear trends indicates that the section-averaged numerical solution is being influenced by capillary end effects. For each simulation, we identify the distance from the inlet (and outlet) where the pressure distribution starts to display deviations from a linear behavior by employing the methodology illustrated in Appendix B. This procedure enables us to identify the size of the inlet and outlet regions affected by capillary end effects, respectively denoted as L^p_{in} and L^p_{out} in the following.

One can note that the profile of time and section-averaged oil saturation should be uniform for the set-up and macroscopically homogeneous porous medium of the kind we analyze. The reference value for oil saturation is in this case associated with the time and volume-averaged oil saturation in the medium, as depicted in Figure 5b for the case A–192h–50%. One can clearly note that large deviations from this value taking place near the inlet and outlet are linked with the influence of capillary end effects. The relative extent from the inlet and outlet boundaries where saturation distribution is affected by such effects can be quantified through the methodology illustrated in Appendix B. In the following, we denote by L^S_{in} and L^S_{out} the size of the inlet and outlet regions affected by capillary end effects, as identified through the numerically evaluated time and section-averaged saturation trend.

We then compute $\overline{\xi}$ by averaging values of $\xi = L^p_{in}, L^p_{out}, L^S_{in}, L^S_{out}$ obtained from each analyzed subsample, while discarding the results associated with subsamples characterized by $l_z = 32h, 64h, 96h, 128h$ that are too small to provide a clear distinction between disturbed and undisturbed trends. The results obtained are summarized in Table IV. For each case, we then consider the largest size between the one identified through the pressure and saturation results as the size of the disturbed region, i.e., $\overline{L}_{in} = \max(\overline{L}^p_{in}, \overline{L}^S_{in})$ and $\overline{L}_{out} = \max(\overline{L}^p_{out}, \overline{L}^S_{out})$. It can be noted that $\overline{L}^i_{in}$ and $\overline{L}^i_{out}$ (with $i = p, S$) obtained via pressure and saturation profiles are similar for most of the cases investigated. Large differences between the values obtained via pressure and saturation profiles are evidenced for the largest value of the integral scale, λ, (i.e., sample C) due to the pronounced oscillations induced by the large variability of the section-averaged porosity. Comparing the results obtained,

TABLE IV: Size of the inlet and outlet regions affected by capillary end effects, as determined by the pressure trend ($\overline{L}_{in}^{p}$ and $\overline{L}_{out}^{p}$) and the saturation trend ($\overline{L}_{in}^{S}$ and $\overline{L}_{out}^{S}$). The values listed are obtained by averaging results obtained across subsamples that are sufficiently large to clearly display undisturbed regions. The actual size of the affected regions ($\overline{L}_{in}$ and $\overline{L}_{out}$) are taken as the maximum value between the pressure- and saturation-based values.

Sample	$S_{o,\mathrm{inlet}}$	$\overline{L}_{in}^{p}$	$\overline{L}_{in}^{S}$	$\overline{L}_{out}^{p}$	$\overline{L}_{out}^{S}$	$\overline{L}_{in}$	$\overline{L}_{out}$
A	20%	$18h$	$28h$	$12h$	$18h$	$28h$	$18h$
	50%	$25h$	$36h$	$19h$	$19h$	$36h$	$19h$
	80%	$21h$	$19h$	$16h$	$18h$	$21h$	$18h$
B	20%	$28h$	$26h$	$25h$	$23h$	$28h$	$25h$
	50%	$31h$	$43h$	$32h$	$30h$	$43h$	$32h$
	80%	$27h$	$26h$	$22h$	$30h$	$27h$	$30h$
C	20%	$43h$	$51h$	$38h$	$21h$	$51h$	$38h$
	50%	$30h$	$56h$	$26h$	$31h$	$56h$	$31h$
	80%	$19h$	$51h$	$20h$	$29h$	$51h$	$29h$

the inlet disturbed region is found to be larger than the outlet one. Disturbed regions of increasing size are noticed as the characteristic diameter of the pores increases (i.e., as the integral scale of the pore-space indicator function increases). In general, the inlet oil saturation appears to have a negligible influence on the size of the disturbed regions. However, we note that the latter increase as inlet oil saturation approaches 50%.

Table V lists the ratio between the size of the inlet and outlet disturbed regions averaged over the three inlet oil saturation values, $\overline{\overline{L}}_{in}$ and $\overline{\overline{L}}_{out}$, and λ. Generally speaking, one can note that the size of an inlet disturbed region is comprised between 10 to 19 integral scales λ, the corresponding size at the system outlet being comprised between 8 and 12 integral scales λ.

It is worth emphasizing that additional components can affect the size of the disturbed

TABLE V: Average size of the inlet and outlet regions affected by capillary end effects, as expressed in terms of the integral scale of I, λ.

Sample	$\overline{\overline{L}}_{in}/\lambda$	$\overline{\overline{L}}_{out}/\lambda$
A	18.7	12.0
B	9.8	8.6
C	13.9	8.8

regions. For example, it can be expected the ratio between the capillary pressure and pressure gradient, $p_c/\nabla p$, to have some influence on the capillary end effects. Experiments have documented that increasing the driving force (i.e., ∇p) tends to reduce capillary end effects.[4,5,7,9] The method introduced in Gupta and Maloney[5] to correct steady-state relative permeability data also suggests a dependency of the strength of capillary end effects on the pressure gradient applied and on the bulk capillary pressure of the system. Here, the ratio $p_c/\nabla p$ ranged from 7×10^{-5} m (sample A) to 2×10^{-4} m (sample C). Note that relying solely on the variation of this ratio does not yield an information that enables us to unambiguously identify the impact on the strength of capillary end effects. The characterization of the capillary end effects as a function of $p_c/\nabla p$ will be the subject of future studies.

C. Influence of sample length and capillary end effects on $\overline{S_o}$ and $\overline{k_{r,o}}$

The quantification of the size of the regions affected by capillary end effects enables us to provide an estimate of representative values for global oil saturation and relative permeabilities associated with the samples of diverse lengths analyzed. We do so by either including or excluding the region affected by capillary end effects. These results are depicted in Figure 6, 7, 8 for sample A, B, C, respectively, in terms of time and volume-averaged oil saturation, $\overline{S_o}$, and time averaged oil relative permeabilities, $\overline{k_{r,o}}$, (as defined in Appendix A) as a function of the sample dimensionless length, l_z/h.

Including the areas affected by capillary end effects yields slightly increased values of time and volume-averaged oil saturations since oil accumulates at the inlet region (see Figure 5b). On the other hand, reduced time averaged oil relative permeabilities are obtained when

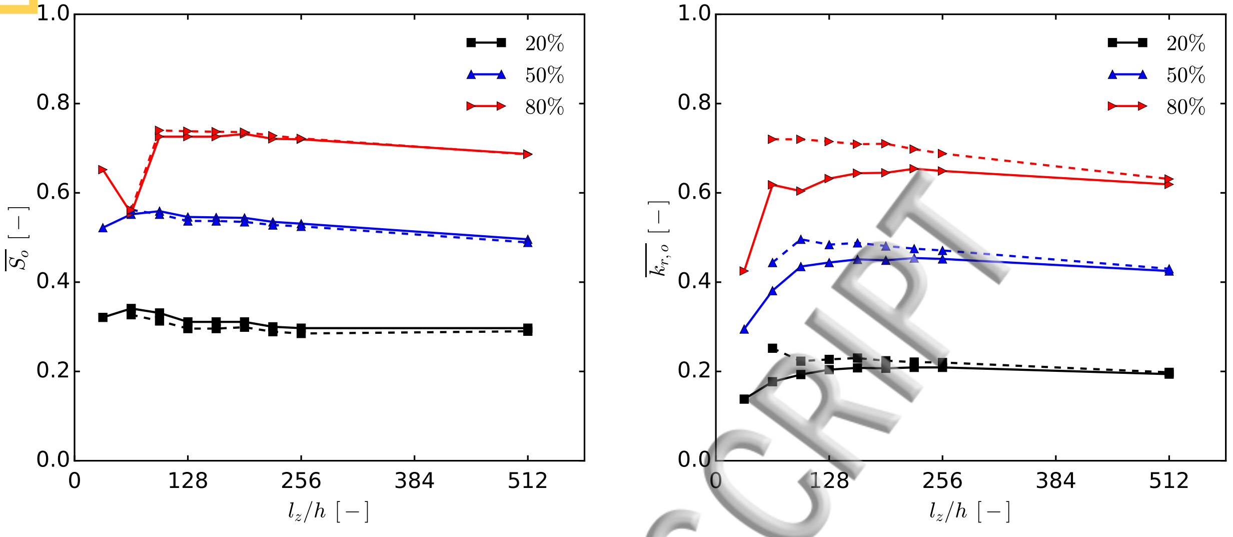

(a) Oil saturation (b) Oil relative permeability

FIG. 6: Values of a) oil saturation and b) oil relative permeability obtained for sample A with diverse inlet oil saturations and sample lengths. Results obtained including or excluding the capillary end effects are respectively denoted by solid or dashed curves.

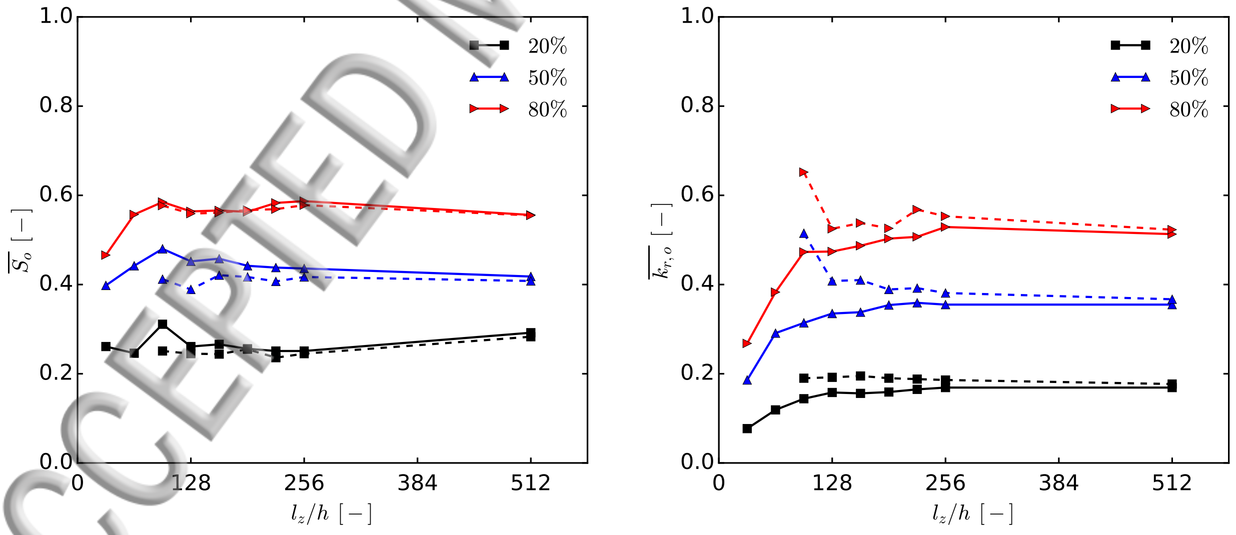

(a) Oil saturation (b) Oil relative permeability

FIG. 7: Values of a) oil saturation and b) oil relative permeability obtained for sample B at diverse inlet oil saturations and sample lengths. Results obtained including or excluding the capillary end effects are respectively denoted by solid or dashed curves.

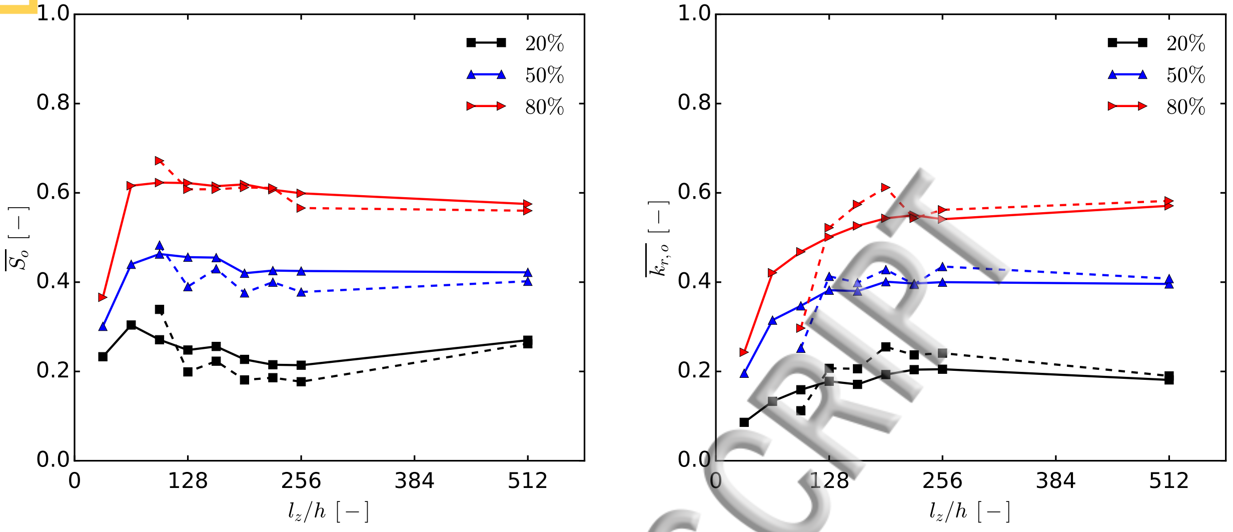

(a) Oil saturation

(b) Oil relative permeability

FIG. 8: Values of a) oil saturation and b) oil relative permeability obtained for sample C at diverse inlet oil saturations and sample lengths. Results obtained including or excluding the capillary end effects are respectively denoted by solid or dashed curves.

capillary end effects are included due to the observation that the overall pressure gradient is higher in this case so that the capillary forces can be overcome at the inlet and outlet. Finally, as the sample length increases, the difference between the two estimates tends to diminish due to the increased extent of the undisturbed region.

Boundary effects are significant (i.e., $\overline{S_o}$ or $\overline{k_{r,o}}$ relative error above 15%) when $l_z < 96h$ for the averaged pore size A and $l_z < 128h$ for the samples B and C. Correspondingly, if the size of the undisturbed region is smaller than approximately 30λ, the inferred oil relative permeability and saturation estimates are not considered to be representative of the sample.

In summary, samples of pore-spaces characterized by an undisturbed region which is too small are problematic with respect to the estimation of consistent relative permeabilities because most of the domain is being influenced by capillary end effects. The need to overcome the effects of capillary forces leads to biased relative permeabilities with respect to the situation where the fluid phases flow in an environment without discontinuities in the solid matrix. When the sample analyzed is large enough, consistent estimates can be obtained, the exclusion of the inlet and outlet disturbed regions from the calculations leading to slightly improved (i.e., more representative) results.

IV. CONCLUSION

The influence of capillary end effects on steady-state relative permeabilities obtained from pore-scale numerical simulations has been investigated. Co-injection of a wetting (water) and a non-wetting (oil) phase has been simulated inside randomly generated three-dimensional porous micro-structures using a finite volume-based solver. Three pore-space samples with diverse pore sizes as well as subsamples of various lengths (along the mean flow direction) have been investigated at three different inlet oil saturations (for a total of 81 test cases).

Similarities with laboratory-scale observations associated with capillary end effects have been evidenced at the pore-scale. Accumulation of the non-wetting phase at the inlet and of the wetting phase at the outlet, resulting from the solid matrix discontinuities, has been consistently observed across the collection of samples analyzed. The relative strength of the capillary end effects was found to depend on the average pore size of the porous system.

Samples that are too small with respect to the integral scale, λ, of the void space are strongly effected by capillary end effects. Estimates of (volume-averaged) oil saturation and relative permeability obtained in these conditions are inconsistent with those obtained in the largest samples, where capillary end effects are negligible and would yield biased results for the dependency of relative permeability curves on fluid saturation.

We quantify the extent of the regions where the influence of capillary end effects is relevant through an approach based on the analysis of the computed trends of time and section-averaged fluid pressure and oil saturation distribution. Our results suggest that relative permeability curves which are not affected by capillary end effects can be obtained by considering simulation results associated with porous micro-structures larger than about 60λ in order to have an inner undisturbed region spanning at least 30λ.

We emphasize that additional components can affect the relative strength of capillary end effects, including, e.g., the ratio between the capillary pressure and pressure gradient, of the order of 10^{-4} m in this study. A detailed analysis of the influence of pore-space geometry and operating conditions on the capillary end effects is the subject of a future study.

ACKNOWLEDGEMENTS

JDH thanks the LANL LDRD Director's Postdoctoral Fellowship Grant # 20150763PRD4 for support. AG and MR acknowledge funding from the European Union's Horizon 2020 Research and Innovation program (Project "Furthering the Knowledge Base for Reducing the Environmental Footprint of Shale Gas Development" FRACRISK, grant agreement 636811).

Appendix A: Post-processing

Analysis of the numerical results is performed through the estimation of section-averaged quantities yielding profiles of the target variables along the direction of the mean flow. For the analysis of relative permeabilities associated with two-phase flow, we are mainly interested in the oil saturation and pressure distribution within the sample. At a height z, the section-averaged values of oil saturation S_o and pressure p are:

$$\langle S_o\rangle_z = \left.\frac{\sum_{i=1}^{N} S_{o,i}V_i}{\sum_{i=1}^{N} V_i}\right|_z \tag{A1}$$

$$\langle p\rangle_z = \left.\frac{\sum_{i=1}^{N} p_iV_i}{\sum_{i=1}^{N} V_i}\right|_z \tag{A2}$$

where N is the number of fluid cells at the given z-coordinate, and $S_{o,i}$, p_i, and V_i are the oil saturation, pressure and volume within the i-th cell, respectively.

Pressure p here is also termed mixture pressure. The section-averaged pressure of the oil, p_o, and water, p_w, phases are evaluated as:

$$\langle p_o\rangle_z = \left.\frac{\sum_{i=1}^{N} p_iS_{o,i}V_i}{\sum_{i=1}^{N} S_{o,i}V_i}\right|_z \tag{A3}$$

$$\langle p_w\rangle_z = \left.\frac{\sum_{i=1}^{N} p_iS_{w,i}V_i}{\sum_{i=1}^{N} S_{w,i}V_i}\right|_z \tag{A4}$$

The time and section-averaged oil saturation and pressures are designated as $\overline{\langle S_o\rangle}_z$, $\overline{\langle p\rangle}_z$, $\overline{\langle p_o\rangle}_z$ and $\overline{\langle p_w\rangle}_z$, respectively. Finally, the time and section-averaged capillary pressure is given as $\overline{\langle p_c\rangle}_z = \overline{\langle p_o\rangle}_z - \overline{\langle p_w\rangle}_z$.

In addition to section-averaged values of oil saturation and pressure, the computation of oil relative permeabilities, $k_{r,o}$, and volume-averaged oil saturations, S_o, are also required.

AIP Publishing

In order to compute these variables, the pore-space located between an initial plane at $z = 0$ and a final plane at $z = l_z$ is considered. The volume-averaged oil saturation is

$$S_o = \frac{\sum_{i=1}^{N_c} S_{o,i} V_i}{\sum_{i=1}^{N_c} V_i} \tag{A5}$$

where N_c is the number of fluid cells satisfying $0 \leq z_i \leq l_z$. The relative oil permeability, is calculated as $k_{r,o} = k_o/k_{\text{abs}}$, with

$$k_o = -\mu_o \, S_{o,\text{inlet}} \, \overline{U} \left(\frac{l_z - h}{\langle p \rangle_{z=l_z} - \langle p \rangle_{z=0}} \right) \tag{A6}$$

k_{abs} being the absolute permeability associated with the system volume comprised between $z = 0$ and $z = l_z$, calculated from a single-phase flow simulation. Note that in (A6) we subtract one voxel size, h, during the calculation of the pressure gradient because pressures are evaluated at the cell center. As a result of the numerical simulation set-up, the inlet velocity, $\overline{U}$, and the inlet oil saturation, $S_{o,\text{inlet}}$, are constant. Hence the water relative permeability is directly proportional to the oil relative permeability (i.e., $k_{r,w} = \mu_w(1 - S_{o,\text{inlet}})/(\mu_o S_{o,\text{inlet}})k_{r,o}$). Hereafter, the computation of the water relative permeability is therefore omitted and only oil relative permeabilities are presented. The time and volume-averaged oil saturation and the time averaged oil relative permeability are respectively denoted as $\overline{S_o}$ and $\overline{k_{r,o}}$.

Appendix B: Estimation of disturbed regions size

The following steps are performed to obtain an estimate of L_{in}^p:

- **Undisturbed trend:** fit the numerically evaluated time and section-averaged water and oil pressures against

$$\overline{\langle p_w \rangle}_z = (\nabla p) z + \overline{\langle p_w \rangle}_0 \tag{B1}$$

$$\overline{\langle p_o \rangle}_z = (\nabla p) z + \overline{\langle p_o \rangle}_0 \tag{B2}$$

to obtain ∇p, $\overline{\langle p_w \rangle}_0$ and $\overline{\langle p_o \rangle}_0$.

- **Subset trend:** fit the numerically evaluated time and section-averaged water and oil pressures against linear trends of the kind

$$\overline{\langle p_w \rangle}_z = (\widetilde{\nabla p})_k z + \overline{\langle p_w \rangle}_0 \tag{B3}$$

AIP Publishing

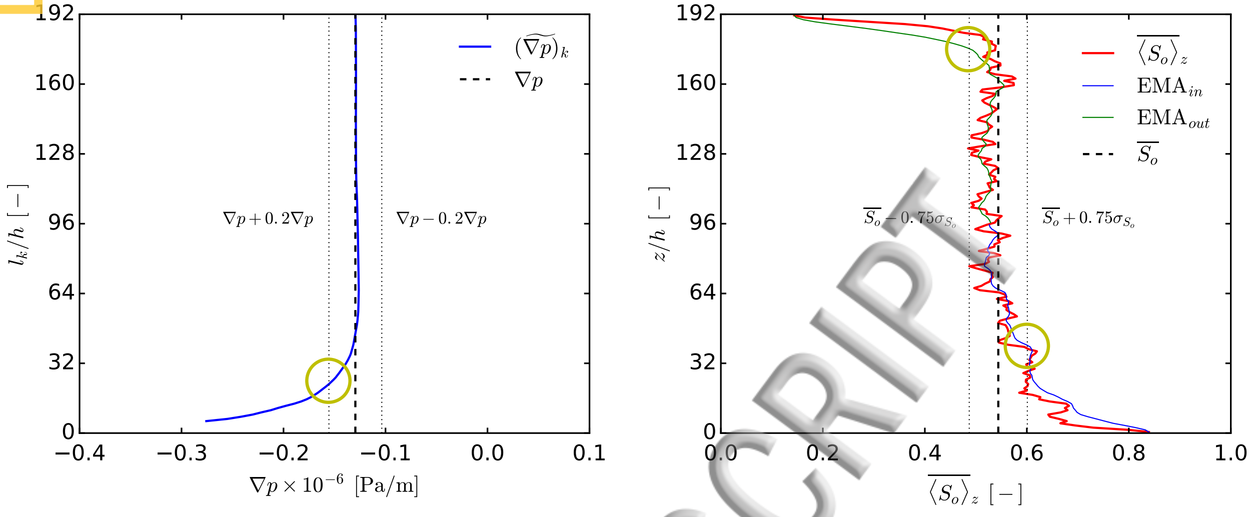

(a) Pressure-based (inlet)

(b) Saturation-based

FIG. 9: Determination of the size of the disturbed regions for case A–192h–50% according to a) pressure-based and b) saturation-based methods.

$$\overline{\langle p_o\rangle_z} = (\widetilde{\nabla p})_k z + \overline{\langle p_o\rangle_0} \tag{B4}$$

respectively for water and oil, to obtain $(\widetilde{\nabla p})_k$. Here, $k = 5...l_z/h$ denoted subsample of length $l_k = kh$ (evaluated starting from $z = 0$). We define $(L^p_{in})^{\theta_p} = l_k$ for the minimum value of k such as $|(\widetilde{\nabla p})_k - \nabla p| < \theta_p \nabla p$, with θ_p a given threshold.

- **Averaging:** to obtain stable results, we then average the values of $(L^p_{in})^{\theta_p}$ obtained from two thresholds, i.e.:

$$L^p_{in} = \frac{(L^p_{in})^{20\%} + (L^p_{in})^{30\%}}{2} \tag{B5}$$

Figure 9a illustrates the procedure by displaying the undisturbed pressure gradient, ∇p, (obtained through the first step above), the threshold values and the fitted pressure gradient on the various subsamples of length l_k. The intersection with the thresholds is identified by a circle in the figure. The assessment of L^p_{out} is performed in a similar way.

Evaluation of L^S_{in} and L^S_{out} is achieved by analyzing the oil saturation distribution and exponential moving averages that start from the inlet and outlet, respectively. The following steps are performed to get L^S_{in}:

- **Undisturbed trend:** the time and volume-averaged oil saturation, $\overline{S_o}$, is calculated.

- **Local trend:** in the cases studied, a good proxy of the local trend of the time and section-averaged oil saturation is given by its exponential moving average (EMA) approximation. It is preferable to use a moving average rather than the raw distribution due to the local oscillations that can alter significantly the identification in some cases. An EMA approximation of time and section-averaged oil saturations is obtained as

$$\mathrm{EMA}_{in}(z=kh)=\begin{cases}\overline{\langle S_o\rangle}_{z=0} & k=0\\ \alpha\overline{\langle S_o\rangle}_{z=kh}+(1-\alpha)\mathrm{EMA}_{in}(z=(k-1)h) & k>0\end{cases}\tag{B6}$$

while the EMA starting from the outlet is given as

$$\mathrm{EMA}_{out}(z=l_z-kh)=\begin{cases}\overline{\langle S_o\rangle}_{z=l_z} & k=0\\ \alpha\overline{\langle S_o\rangle}_{z=l_z-kh}+(1-\alpha)\mathrm{EMA}_{out}(z=l_z-(k-1)h) & k>0\end{cases}\tag{B7}$$

with the weighting coefficient $\alpha=2/(6\lambda+1)$. $(L_{in}^S)^{\theta_S}$ is obtained when EMA_{in} first intersects the threshold $\overline{S_o}+\theta_S\sigma_{S_o}$, σ_{S_o} being the standard deviation of $\overline{\langle S_o\rangle}_z$, while $(L_{out}^S)^{\theta_S}$ is obtained when EMA_{out} first intersects the threshold $\overline{S_o}-\theta_S\sigma_{S_o}$.

- **Averaging:** to obtain stable results, we then average the values of $(L_{in}^S)^{\theta_S}$ obtained from two thresholds, i.e.:

$$L_{in}^S=\frac{(L_{in}^S)^{75\%}+(L_{in}^S)^{100\%}}{2}\tag{B8}$$

The assessment of L_{out}^S is performed in a similar way.

Figure 9b illustrates the procedure by displaying the time and volume-averaged oil saturation, $\overline{S_o}$, the threshold values and the exponential moving averages EMA_{in} and EMA_{out}. The intersections with the thresholds are identified by circles in the figure.

REFERENCES

[1] J. Hyman, J. Jiménez-Martínez, H. Viswanathan, J. Carey, M. Porter, E. Rougier, S. Karra, Q. Kang, L. Frash, L. Chen, *et al.*, "Understanding hydraulic fracturing: a multi-scale problem," Phil. Trans. R. Soc. A **374**, 20150426 (2016).

[2] C. Jenkins, A. Chadwick, and S. D. Hovorka, "The state of the art in monitoring and verification—ten years on," Int. J. Greenhouse Gas Control **40**, 312–349 (2015).

[3] R. S. Middleton, J. W. Carey, R. P. Currier, J. D. Hyman, Q. Kang, S. Karra, J. Jiménez-Martínez, M. L. Porter, and H. S. Viswanathan, "Shale gas and non-aqueous fracturing fluids: Opportunities and challenges for supercritical CO_2," Appl. Energy **147**, 500–509 (2015).

[4] M. Leverett, "Capillary behavior in porous solids," Transactions of the AIME **142**, 152–169 (1941).

[5] R. Gupta and D. R. Maloney, "Intercept method–A novel technique to correct steady-state relative permeability data for capillary end effects," SPE Reservoir Evaluation & Engineering **19**, 316–330 (2016).

[6] J. Osoba, J. Richardson, J. Kerver, J. Hafford, and P. Blair, "Laboratory measurements of relative permeability," J. Pet. Technol. **3**, 47–56 (1951).

[7] J. Kyte and L. Rapoport, "Linear waterflood behavior and end effects in water-wet porous media," J. Pet. Technol. **10**, 47–50 (1958).

[8] M. Moura, E.-A. Fiorentino, K. J. Måløy, G. Schfer, and R. Toussaint, "Impact of sample geometry on the measurement of pressure-saturation curves: Experiments and simulations," Water Resour. Res. **51**, 8900–8926 (2015).

[9] L. Moghadasi, A. Guadagnini, F. Inzoli, M. Bartosek, and D. Renna, "Characterization of two- and three-phase relative permeability of water-wet porous media through X-Ray saturation measurements," J. Pet. Sci. Eng. **145**, 453–463 (2016).

[10] E. F. Johnson, D. P. Bossler, and V. O. Naumann, "Calculation of relative permeability from displacement experiments," Petroleum Transactions, AIME **216**, 370–372 (1959).

[11] L. Moghadasi, A. Guadagnini, F. Inzoli, and M. Bartosek, "Interpretation of two-phase relative permeability curves through multiple formulations and model quality criteria," J. Pet. Sci. Eng. **135**, 738–749 (2015).

[12] B. Maini, G. Coskuner, and K. Jha, "A comparison of steady-state and unsteady-state relative permeabilities of viscocities oil and water in ottawa sand," J. Can. Pet. Technol. **29** (1990), 10.2118/90-02-02.

[13] M. J. Blunt, "Flow in porous media — pore-network models and multiphase flow," Curr. Opin. Colloid Interface Sci. **6**, 197–207 (2001).

[14] M. J. Blunt, M. D. Jackson, M. Piri, and P. H. Valvatne, "Detailed physics, predictive capabilities and macroscopic consequences for pore-network models of multiphase flow," Adv. Water Resour. **25**, 1069–1089 (2002).

[15] M. Piri and M. J. Blunt, "Three-dimensional mixed-wet random pore-scale network modeling of two- and three-phase flow in porous media. I. Model description," Phys. Rev. E **71**, 026301 (2005).

[16] P. H. Valvatne, M. Piri, X. Lopez, and M. J. Blunt, "Predictive pore-scale modeling of single and multiphase flow," Transp. Porous Media **58**, 23–41 (2005).

[17] A. V. Ryazanov, M. I. van Dijke, and K. S. Sorbie, "Pore-network prediction of residual oil saturation based on oil layer drainage in mixed-wet systems," in *SPE Improved Oil Recovery Symposium, 24-28 April, Tulsa, Oklahoma, USA* (Society of Petroleum Engineers (SPE), 2010).

[18] A. Al-dhahli, S. Geiger, and M. I. van Dijke, "Accurate modelling of pore-scale film and layer flow for three-phase EOR in carbonate rocks with arbitrary wettability," in *SPE Improved Oil Recovery Symposium, 14-18 April, Tulsa, Oklahoma, USA* (Society of Petroleum Engineers (SPE), 2012).

[19] P. Meakin and A. M. Tartakovsky, "Modeling and simulation of pore-scale multiphase fluid flow and reactive transport in fractured and porous media," Rev. Geophys. **47**, RG3002 (2009).

[20] A. Q. Raeini, M. J. Blunt, and B. Bijeljic, "Modelling two-phase flow in porous media at the pore scale using the volume-of-fluid method," J. Comput. Phys. **231**, 5653–5668 (2012).

[21] T. Arrufat, I. Bondino, S. Zaleski, B. Lagrée, and N. Keskes, "Developments on relative permeability computation in 3D rock images," in *Abu Dhabi International Petroleum Exhibition and Conference, 10-13 November, Abu Dhabi, UAE* (Society of Petroleum Engineers (SPE), 2014).

[22]A. Q. Raeini, B. Bijeljic, and M. J. Blunt, “Numerical modelling of sub-pore scale events in two-phase flow through porous media,” Transp. Porous Media **101**, 191–213 (2014).

[23]A. Q. Raeini, M. J. Blunt, and B. Bijeljic, “Direct simulations of two-phase flow on micro-CT images of porous media and upscaling of pore-scale forces,” Adv. Water Resour. **74**, 116–126 (2014).

[24]A. Q. Raeini, B. Bijeljic, and M. J. Blunt, “Modelling capillary trapping using finite-volume simulation of two-phase flow directly on micro-CT images,” Adv. Water Resour. **83**, 102–110 (2015).

[25]O. Dinariev and N. Evseev, “Multiphase flow modeling with density functional method,” Comput. Geosci. **20**, 835–856 (2016).

[26]A. M. Tartakovsky, A. L. Ward, and P. Meakin, “Pore-scale simulations of drainage of heterogeneous and anisotropic porous media,” Physics of Fluids **19**, 103301 (2007).

[27]H. Huang and X. yun Lu, “Relative permeabilities and coupling effects in steady-state gas-liquid flow in porous media: A lattice boltzmann study,” Physics of Fluids **21**, 092104 (2009).

[28]H. Liu, Y. Zhang, and A. J. Valocchi, “Lattice boltzmann simulation of immiscible fluid displacement in porous media: Homogeneous versus heterogeneous pore network,” Physics of Fluids **27**, 052103 (2015).

[29]H. Liu, Q. Kang, C. R. Leonardi, S. Schmieschek, A. Narváez, B. D. Jones, J. R. Williams, A. J. Valocchi, and J. Harting, “Multiphase lattice Boltzmann simulations for porous media applications,” Comput. Geosci. **20**, 777–805 (2016).

[30]J. O. Helland and E. Jettestuen, “Mechanisms for trapping and mobilization of residual fluids during capillary-dominated three-phase flow in porous rock,” Water Resour. Res. **52**, 5376–5392 (2016).

[31]P. Mohammadmoradi and A. Kantzas, “Petrophysical characterization of porous media starting from micro-tomographic images,” Adv. Water Resour. **94**, 200–216 (2016).

[32]T. Ramstad, N. Idowu, C. Nardi, and P.-E. Øren, “Relative permeability calculations from two-phase flow simulations directly on digital images of porous rocks,” Transp. Porous Media **94**, 487–504 (2012).

[33]M. Siena, J. D. Hyman, M. Riva, A. Guadagnini, C. L. Winter, P. K. Smolarkiewicz, P. Gouze, S. Sadhukhan, F. Inzoli, G. Guédon, and E. Colombo, “Direct numerical simulation of fully saturated flow in natural porous media at the pore scale: a comparison of

AIP Publishing

three computational systems," Comput. Geosci. **19**, 423–437 (2015).

[34]D. Wildenschild, K. A. Culligan, and B. S. B. Christensen, "Application of X-ray microtomography to environmental fluid flow problems." in *Developments in X-Ray Tomography IV*, Vol. 5535, edited by U. Bonse (SPIE-Intl Soc Optical Eng, 2004) pp. 432–441.

[35]D. Wildenschild and A. P. Sheppard, "X-ray imaging and analysis techniques for quantifying pore-scale structure and processes in subsurface porous medium systems," Adv. Water Resour. **51**, 217–246 (2013).

[36]C. Soulaine, F. Gjetvaj, C. Garing, S. Roman, A. Russian, P. Gouze, and H. A. Tchelepi, "The impact of sub-resolution porosity of x-ray microtomography images on the permeability," Transp. Porous Media **113**, 227–243 (2016).

[37]P. Iassonov, T. Gebrenegus, and M. Tuller, "Segmentation of X-ray computed tomography images of porous materials: A crucial step for characterization and quantitative analysis of pore structures," Water Resour. Res. **45**, W09415 (2009).

[38]P. K. Smolarkiewicz and C. L. Winter, "Pores resolving simulation of Darcy flows," J. Comput. Phys. **229**, 3121–3133 (2010).

[39]J. D. Hyman and C. L. Winter, "Stochastic generation of explicit pore structures by thresholding Gaussian random fields," J. Comput. Phys. **277**, 16–31 (2014).

[40]J. D. Hyman, A. Guadagnini, and C. L. Winter, "Statistical scaling of geometric characteristics in stochastically generated pore microstructures," Comput. Geosci. **19**, 845–854 (2015).

[41]A. Guadagnini, M. J. Blunt, M. Riva, and B. Bijeljic, "Statistical scaling of geometric characteristics in millimeter scale natural porous media," Transp. Porous Media **101**, 465–475 (2014).

[42]J. D. Hyman, P. K. Smolarkiewicz, and C. L. Winter, "Heterogeneities of flow in stochastically generated porous media," Phys. Rev. E **86**, 056701 (2012).

[43]J. D. Hyman, P. K. Smolarkiewicz, and C. L. Winter, "Pedotransfer functions for permeability: A computational study at pore scales," Water Resour. Res. **49**, 2080–2092 (2013).

[44]J. D. Hyman and C. L. Winter, "Hyperbolic regions in flows through three-dimensional pore structures," Physical Review E **88**, 063014 (2013).

[45]M. Siena, M. Riva, J. D. Hyman, C. L. Winter, and A. Guadagnini, "Relationship between pore size and velocity probability distributions in stochastically generated porous media," Physical Review E **89**, 013018 (2014).

[46]H. Dong and M. J. Blunt, “Pore-network extraction from micro-computerized-tomography images,” Physical Review E **80**, 036307 (2009).

[47]N. Cressie, *Statistics for spatial data* (John Wiley & Sons, 2015).

[48]C. Hirt and B. Nichols, “Volume of fluid (VOF) method for the dynamics of free boundaries,” J. Comput. Phys. **39**, 201–225 (1981).

[49]S. O. Unverdi and G. Tryggvason, “A front-tracking method for viscous, incompressible, multi-fluid flows,” J. Comput. Phys. **100**, 25–37 (1992).

[50]M. Sussman, P. Smereka, and S. Osher, “A level set approach for computing solutions to incompressible two-phase flow,” J. Comput. Phys. **114**, 146–159 (1994).

[51]J. Brackbill, D. Kothe, and C. Zemach, “A continuum method for modeling surface tension,” J. Comput. Phys. **100**, 335–354 (1992).

[52]*OpenFOAM User Guide 2015, http://openfoam.org/*.

[53]H. Rusche, *Computational Fluid Dynamics of Dispersed Two-Phase Flows at High Phase Fractions*, Ph.D. thesis, Department of Mechanical Engineering, Imperial College of Science, Technology & Medicine, London (2002).

[54]S. S. Deshpande, L. Anumolu, and M. F. Trujillo, “Evaluating the performance of the two-phase flow solver interFoam,” Comput. Sci. Discov. **5**, 014016 (2012).

[55]P. Shen, B. Zhu, X.-B. Li, and Y.-S. Wu, “An experimental study of the influence of interfacial tension on water–oil two-phase relative permeability,” Transp. Porous Media **85**, 505–520 (2010).

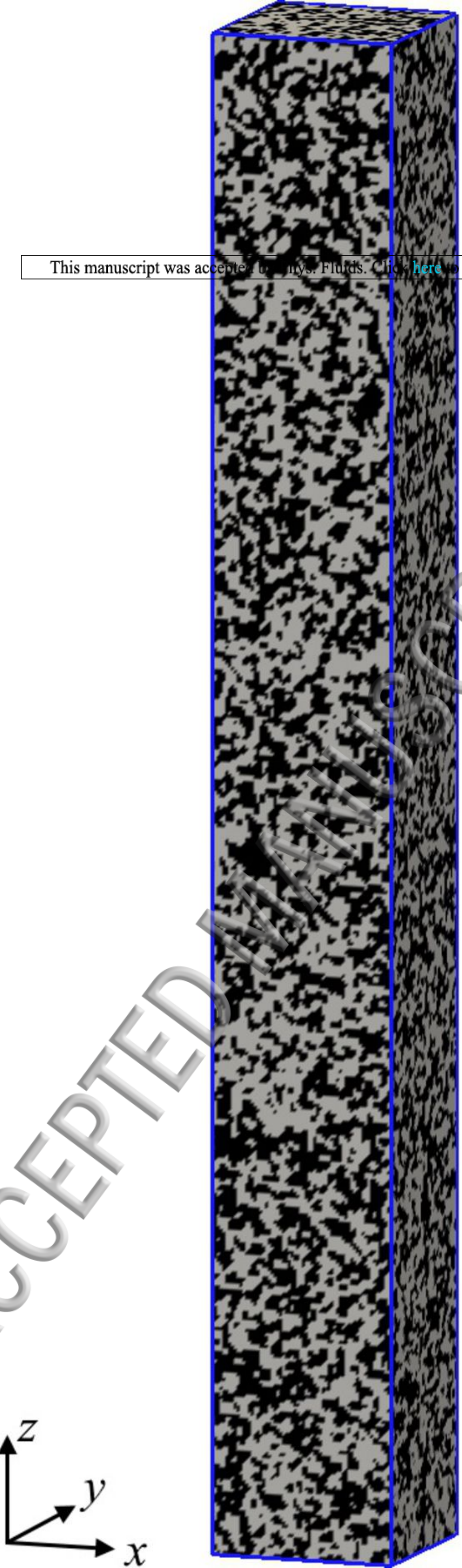
z
y
x

AIP Publishing

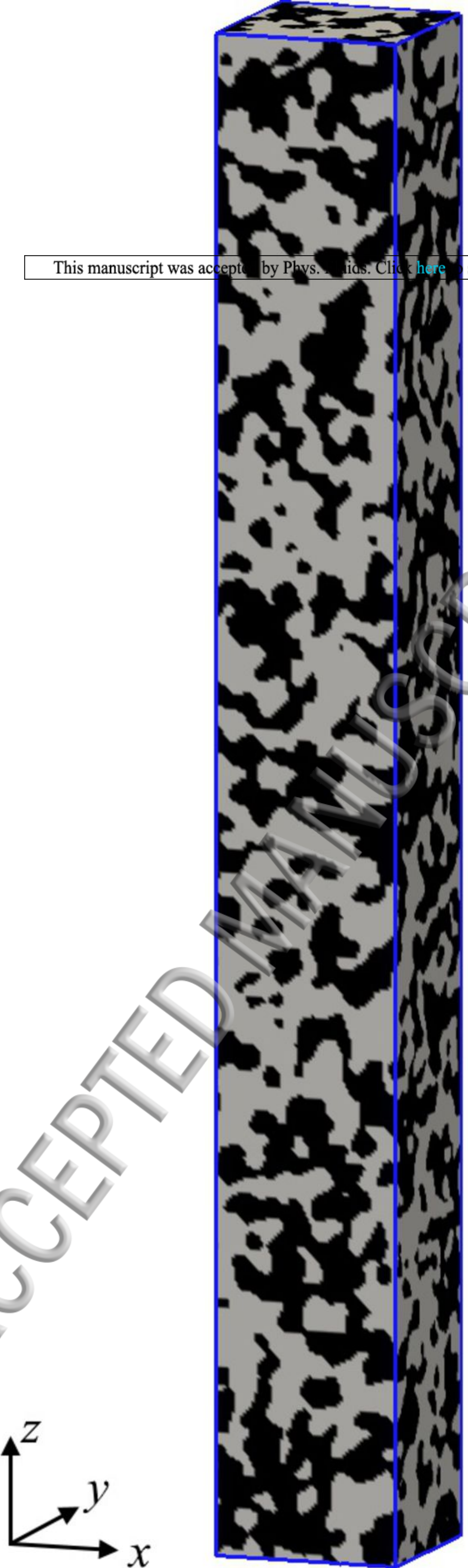

This manuscript was acc d by Phy Fluid Click here o see the version of record.

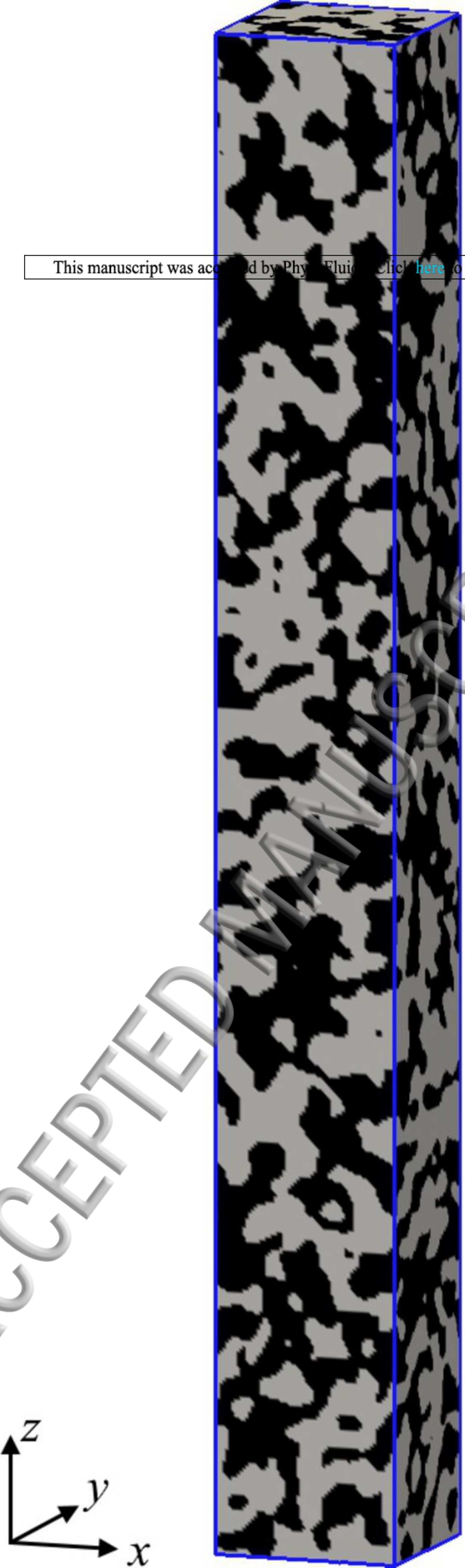

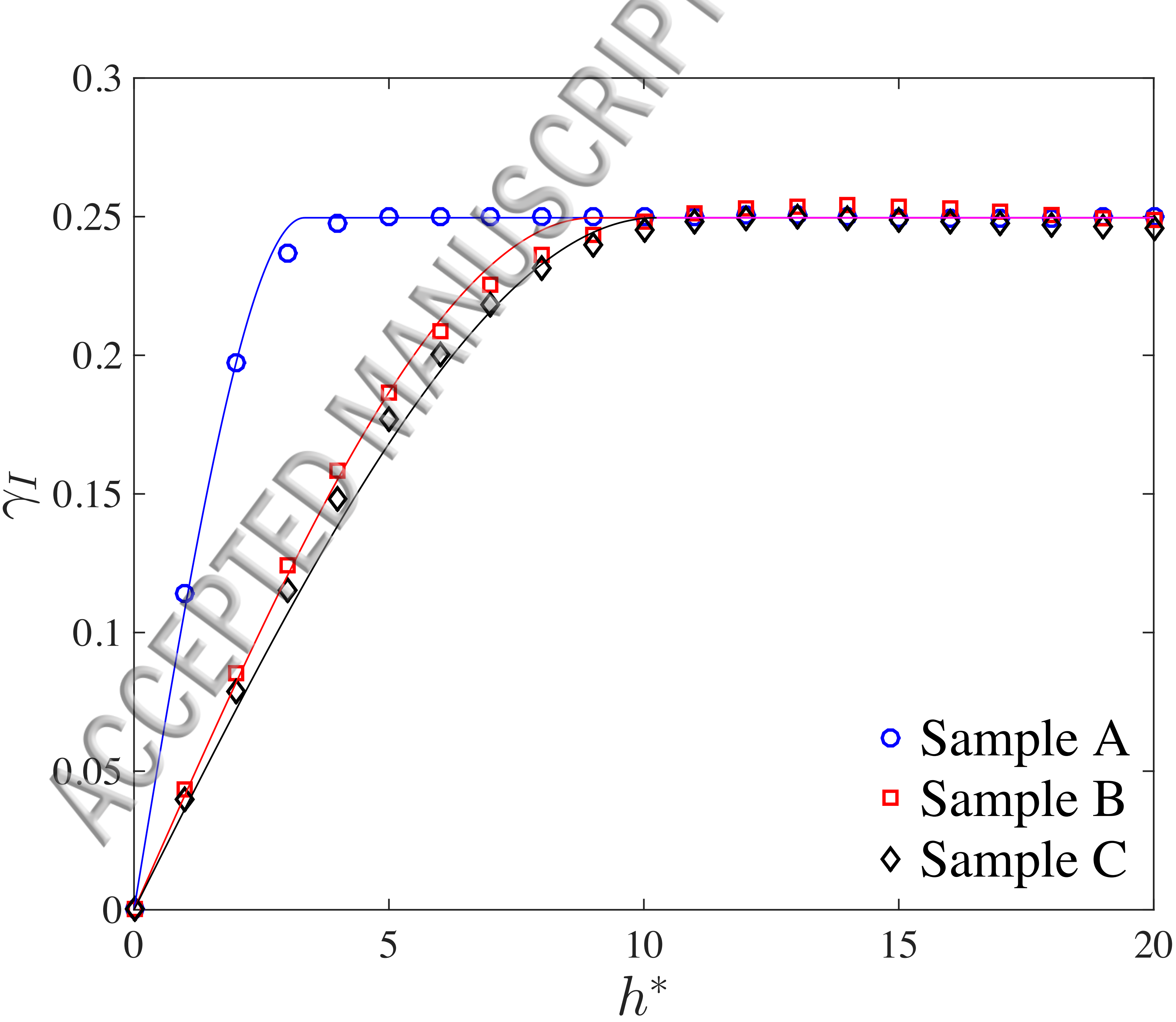

0.3
0.25
0.2
0.15
0.1
0.05
0
γ_I
0
5
10
15
20
h^*
Sample A
Sample B
Sample C

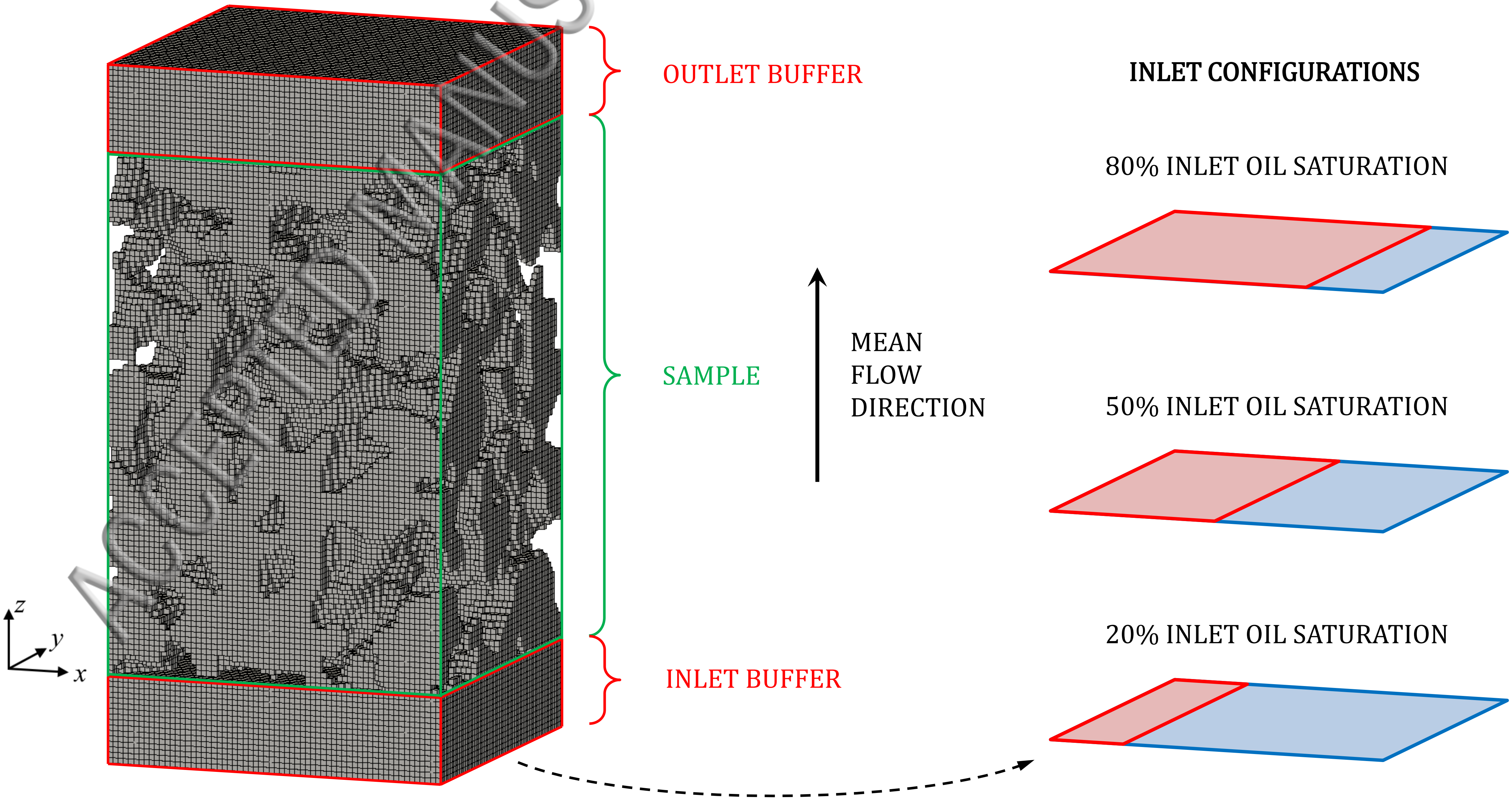
OUTLET BUFFER
SAMPLE
INLET BUFFER
MEAN
FLOW
DIRECTION
INLET CONFIGURATIONS
80% INLET OIL SATURATION
50% INLET OIL SATURATION
20% INLET OIL SATURATION
z
y
x

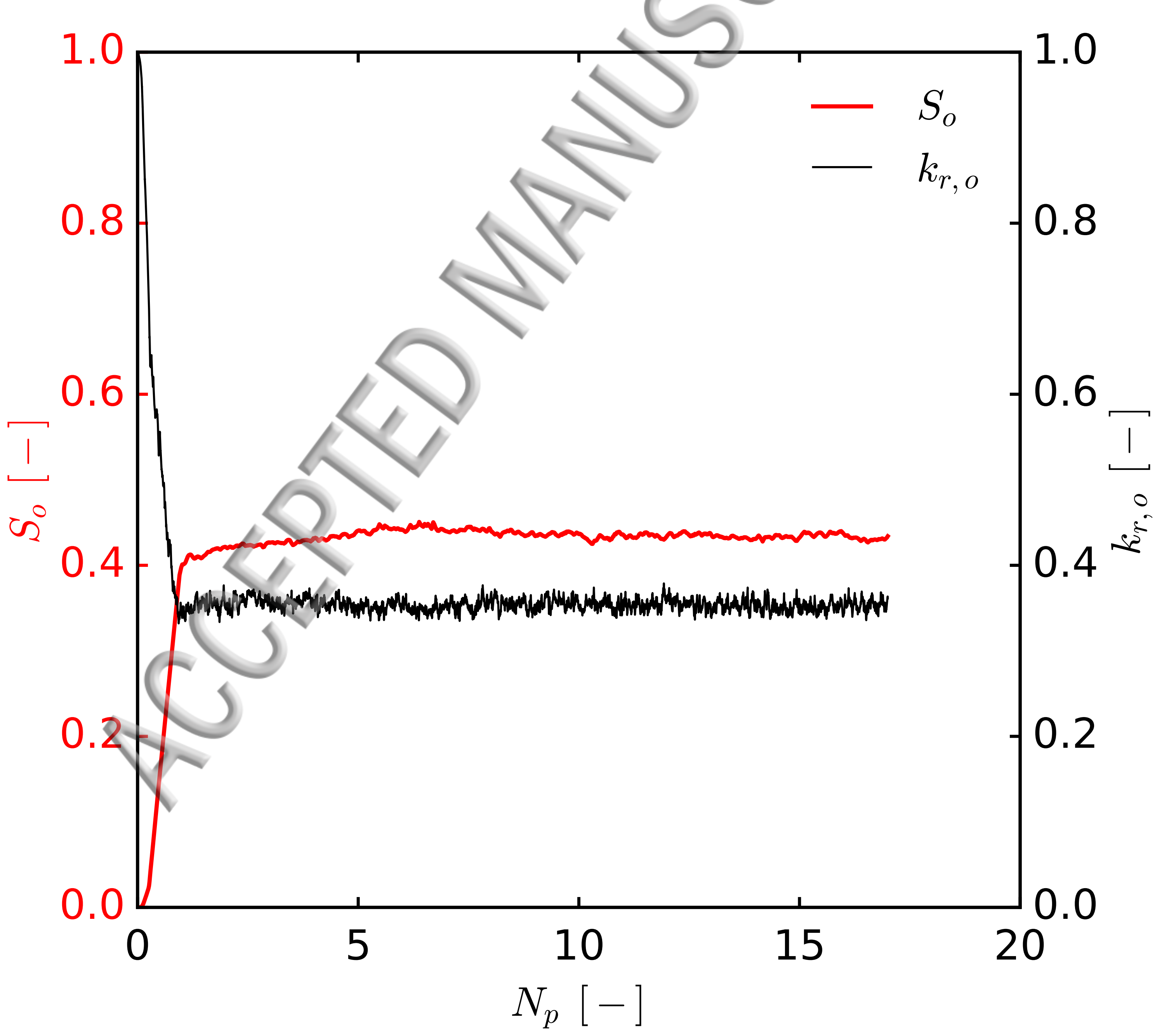

S_o
$k_{r,o}$
$S_o\ [-]$
$k_{r,o}\ [-]$
$N_p\ [-]$
0.0
0.2
0.4
0.6
0.8
1.0
0
5
10
15
20

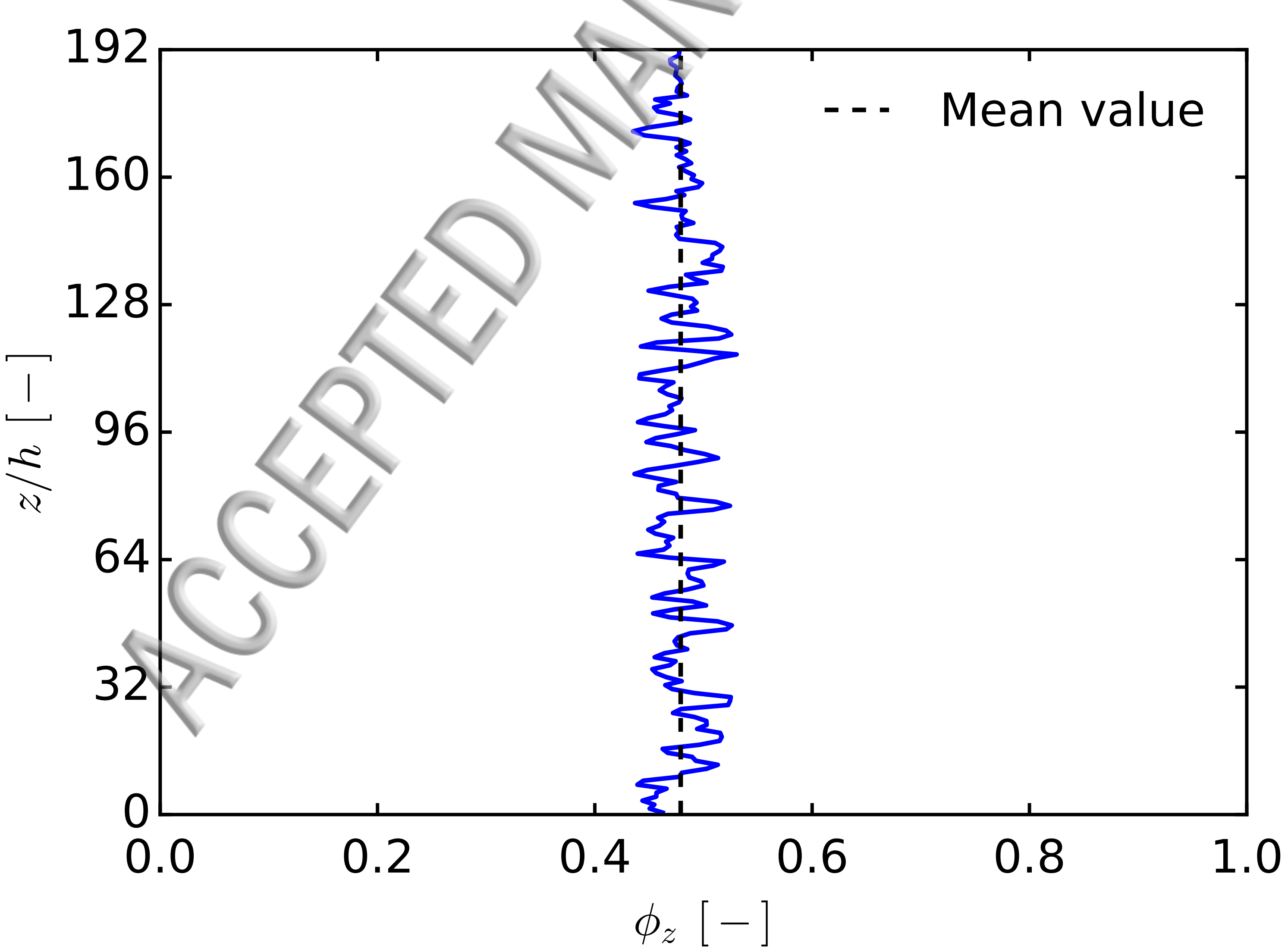

192
160
128
96
64
32
0
$z/h\ [-]$
0.0
0.2
0.4
0.6
0.8
1.0
$\phi_z\ [-]$
Mean value

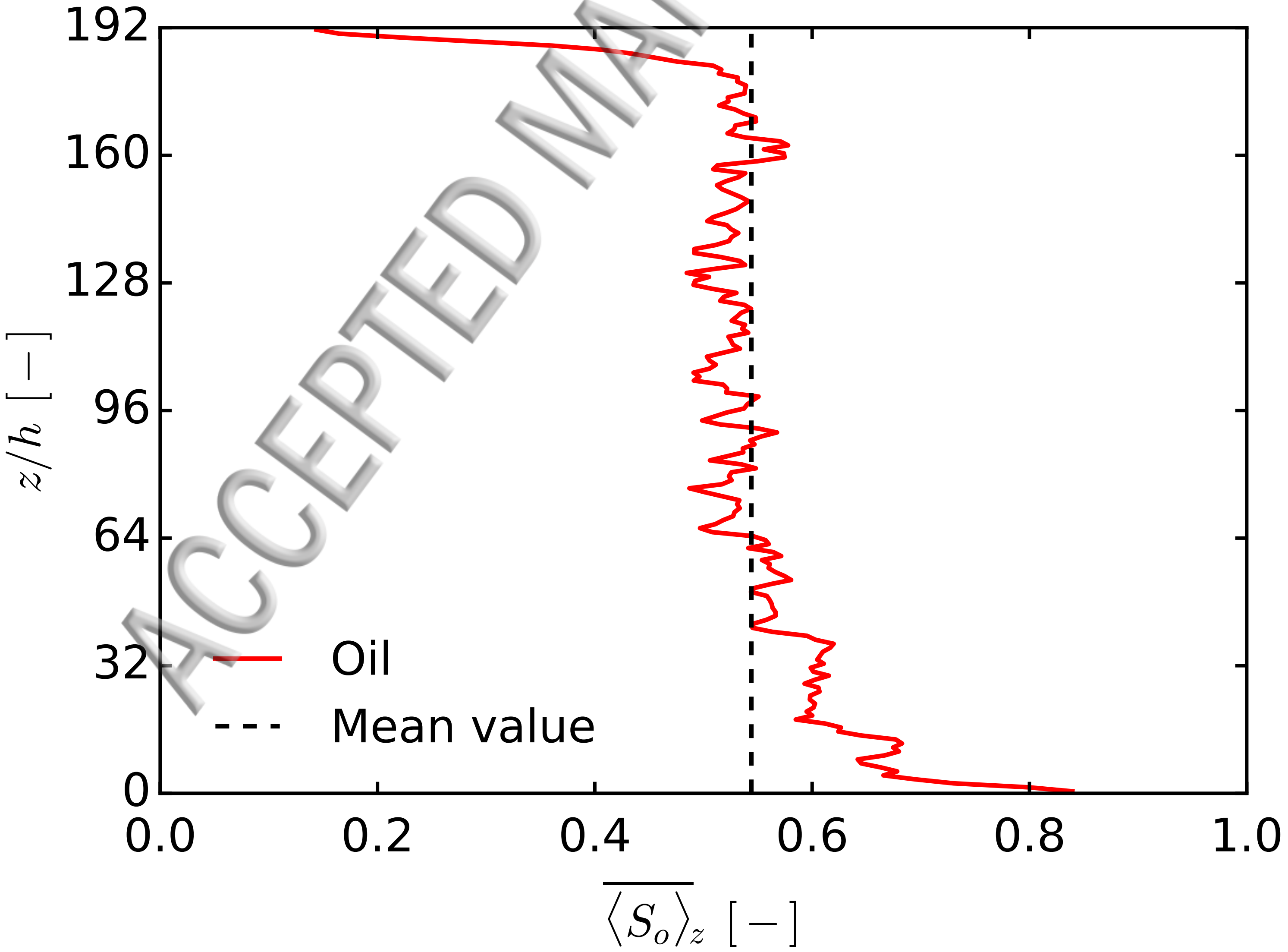
192
160
128
96
64
32
0
0.0
0.2
0.4
0.6
0.8
1.0
$z/h\ [-]$
$\overline{\langle S_o \rangle_z}\ [-]$
Oil
Mean value

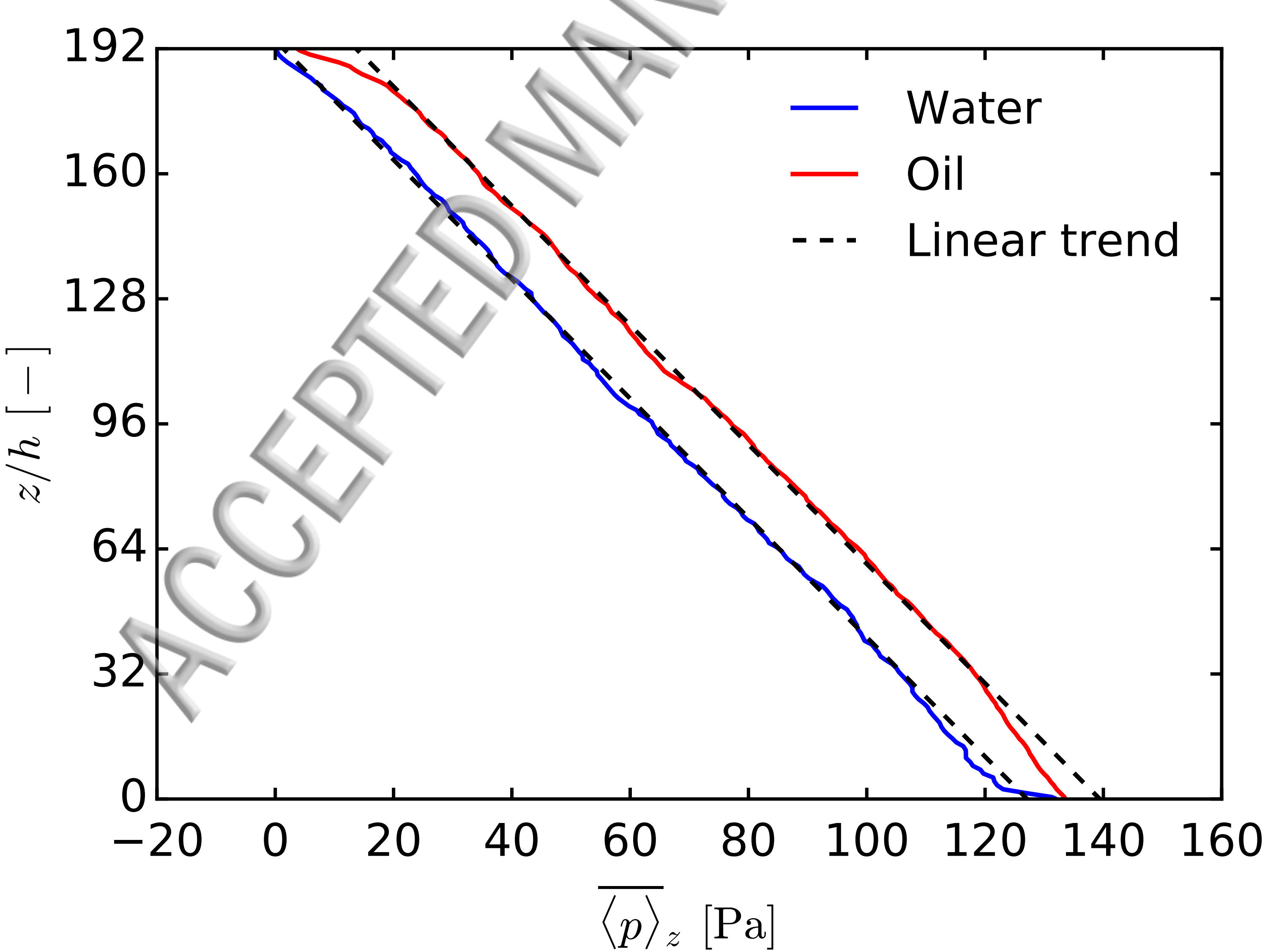
192
160
128
96
64
32
0
−20
0
20
40
60
80
100
120
140
160
$z/h\ [-]$
$\overline{\langle p \rangle}_z\ [\mathrm{Pa}]$
Water
Oil
Linear trend

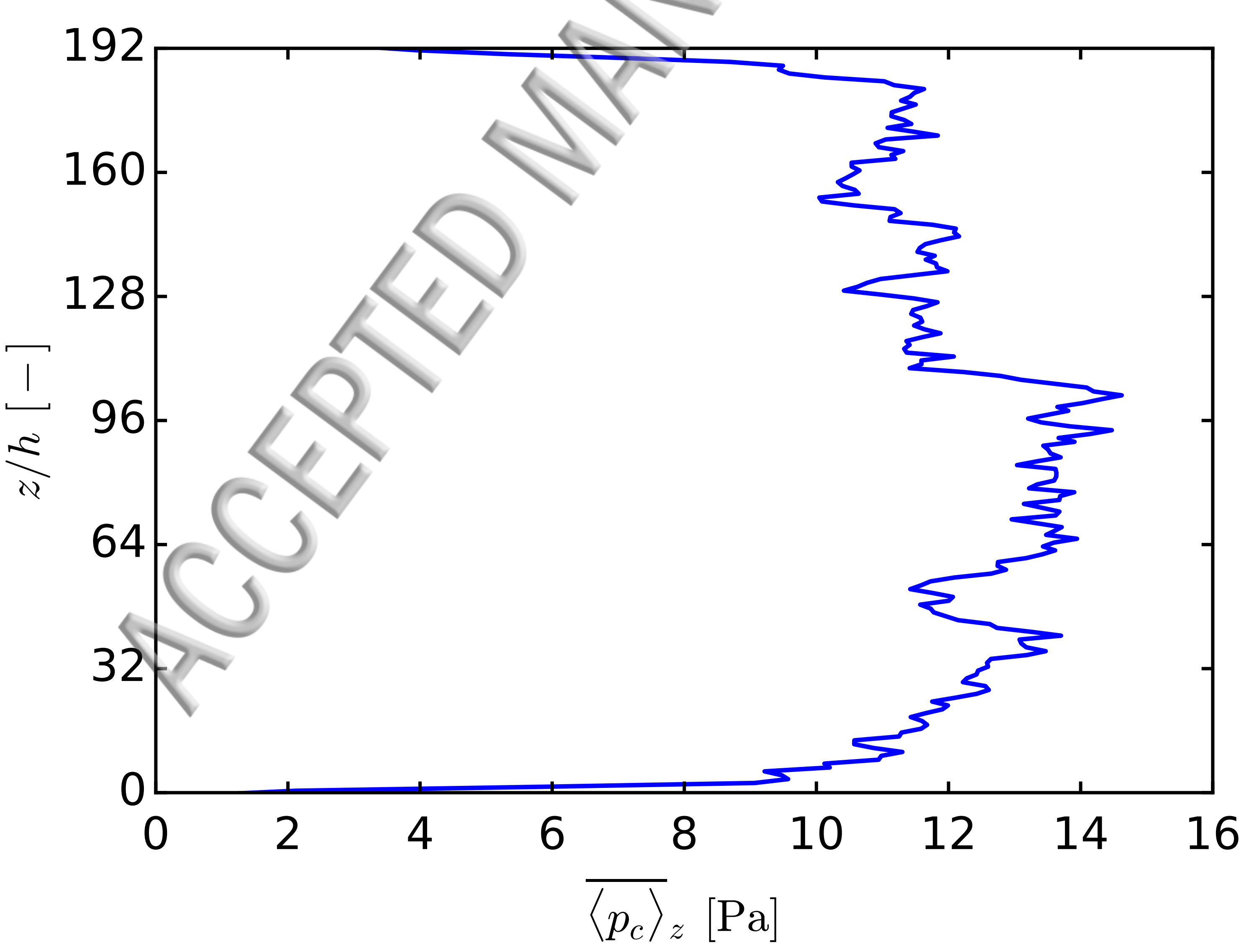
192
160
128
96
64
32
0
$z/h\ [-]$
0
2
4
6
8
10
12
14
16
$\overline{\langle p_c \rangle}_z$ [Pa]

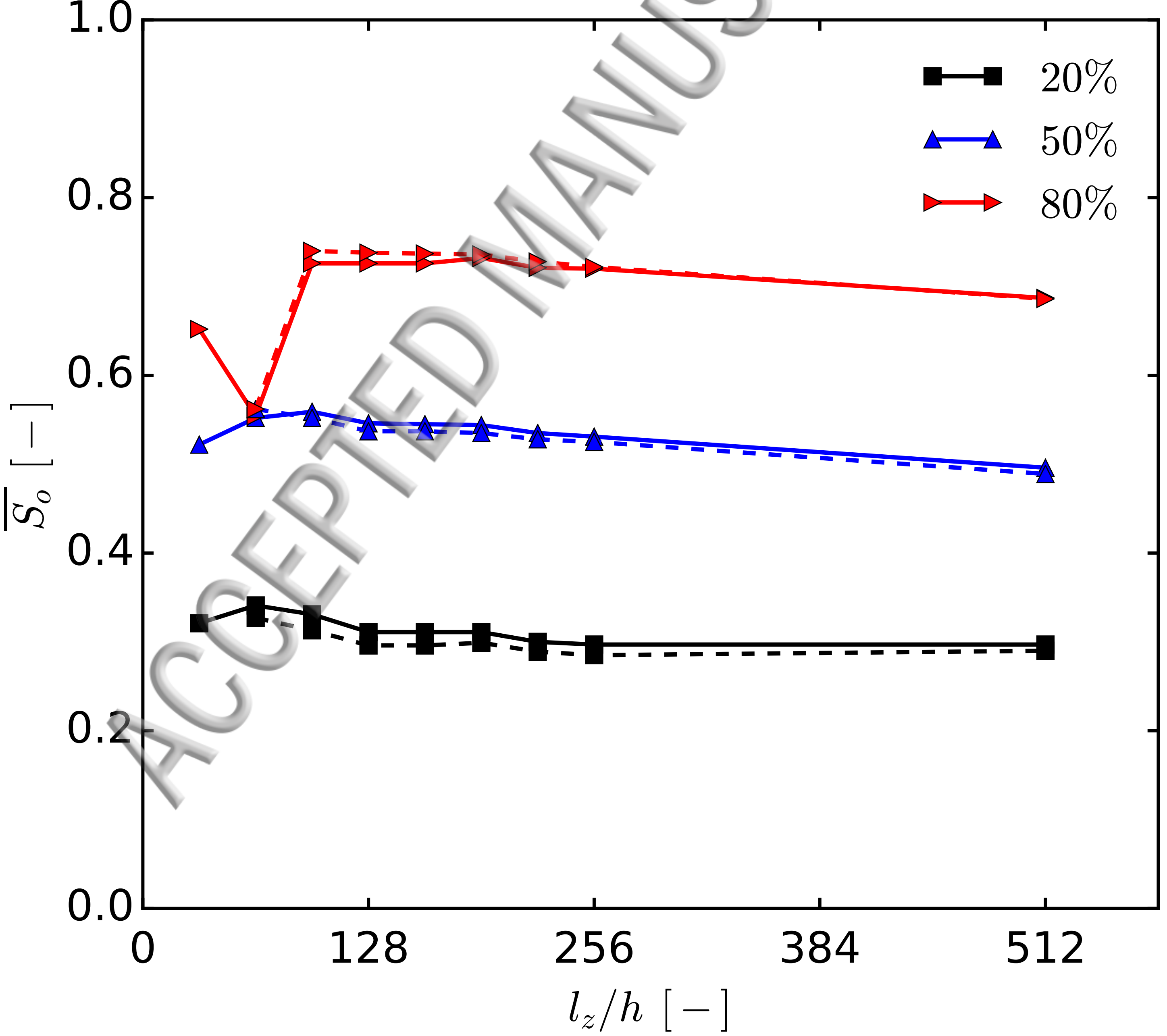
1.0
0.8
0.6
0.4
0.2
0.0
0
128
256
384
512
$l_z/h\ [-]$
$\overline{S_o}\ [-]$
20%
50%
80%

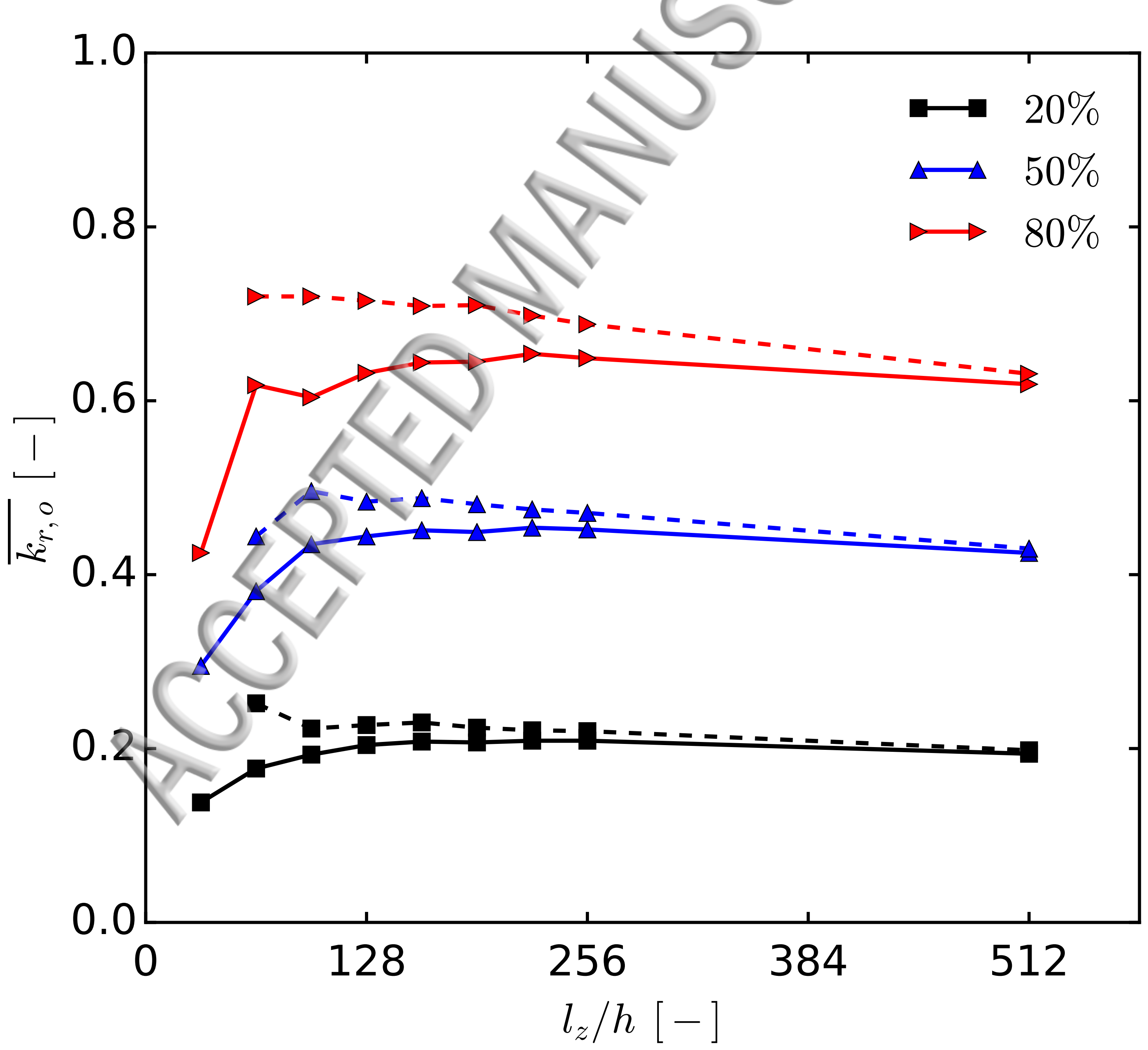
1.0
0.8
0.6
0.4
0.2
0.0
0
128
256
384
512
$l_z/h\ [-]$
$\overline{k_{r,o}}\ [-]$
20%
50%
80%

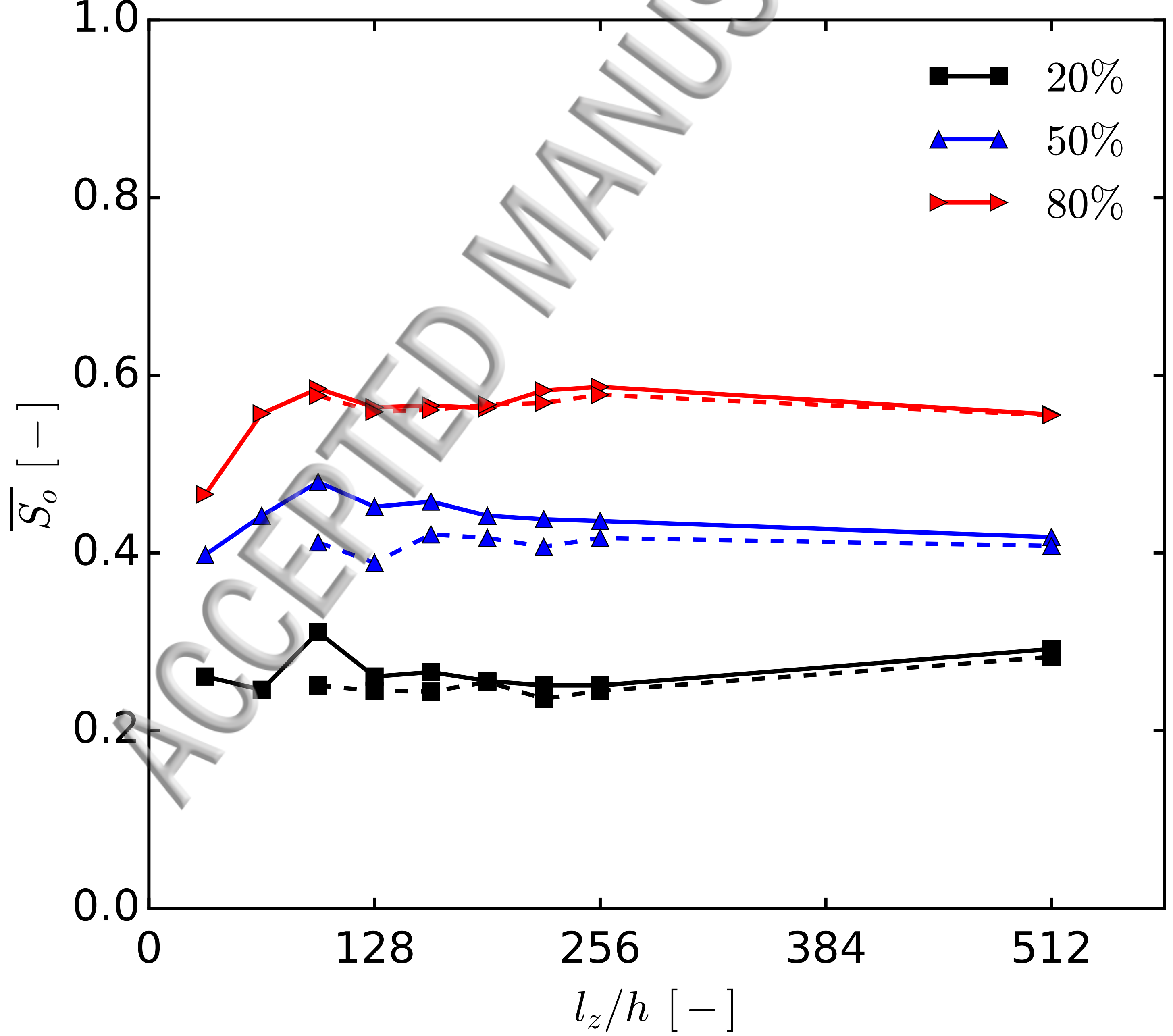

1.0
0.8
0.6
0.4
0.2
0.0
$\overline{S_o}\ [-]$
0
128
256
384
512
$l_z/h\ [-]$
20%
50%
80%

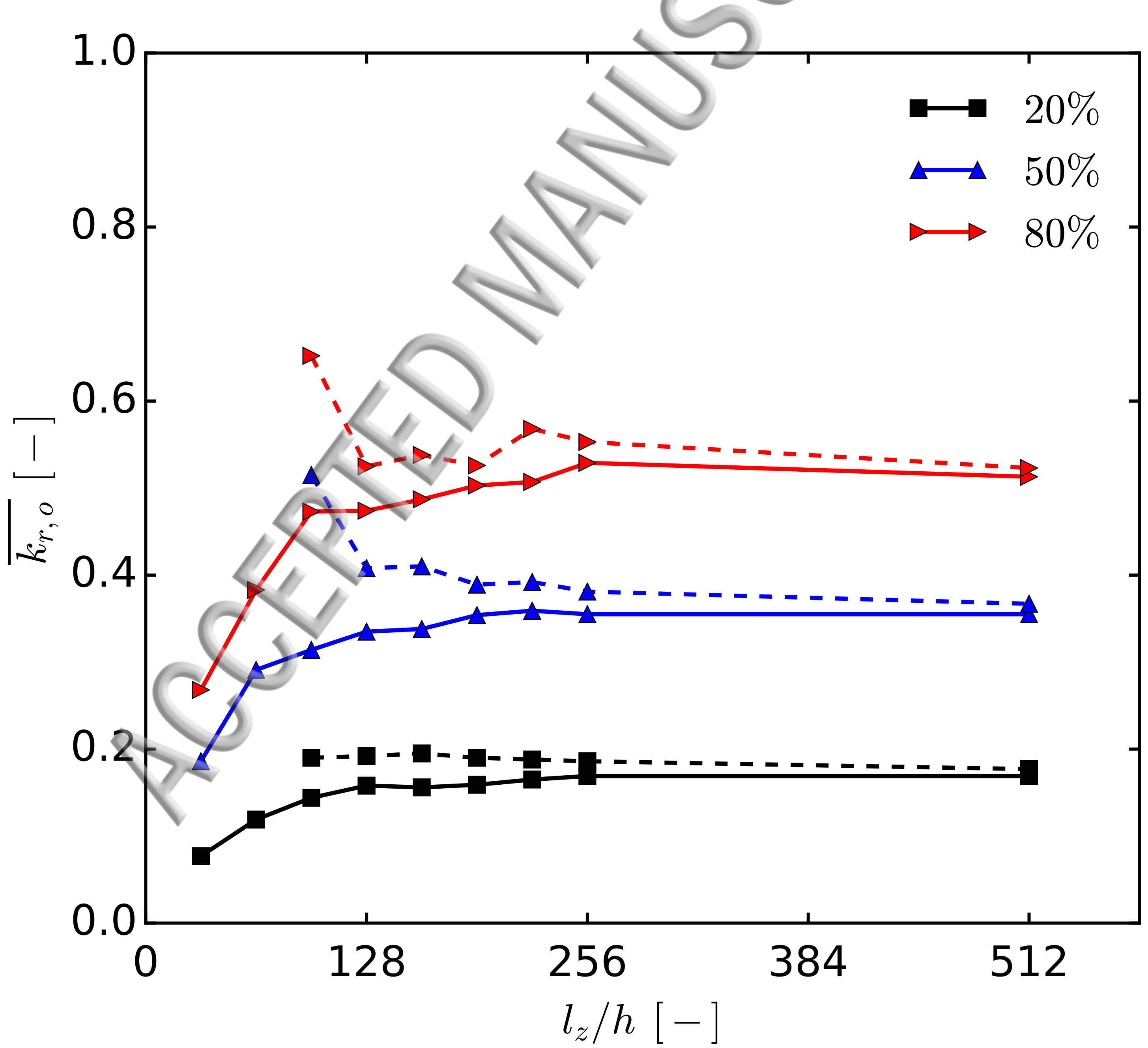
1.0
0.8
0.6
0.4
0.2
0.0
0
128
256
384
512
$\overline{k_{r,o}}\ [-]$
$l_z/h\ [-]$
20%
50%
80%

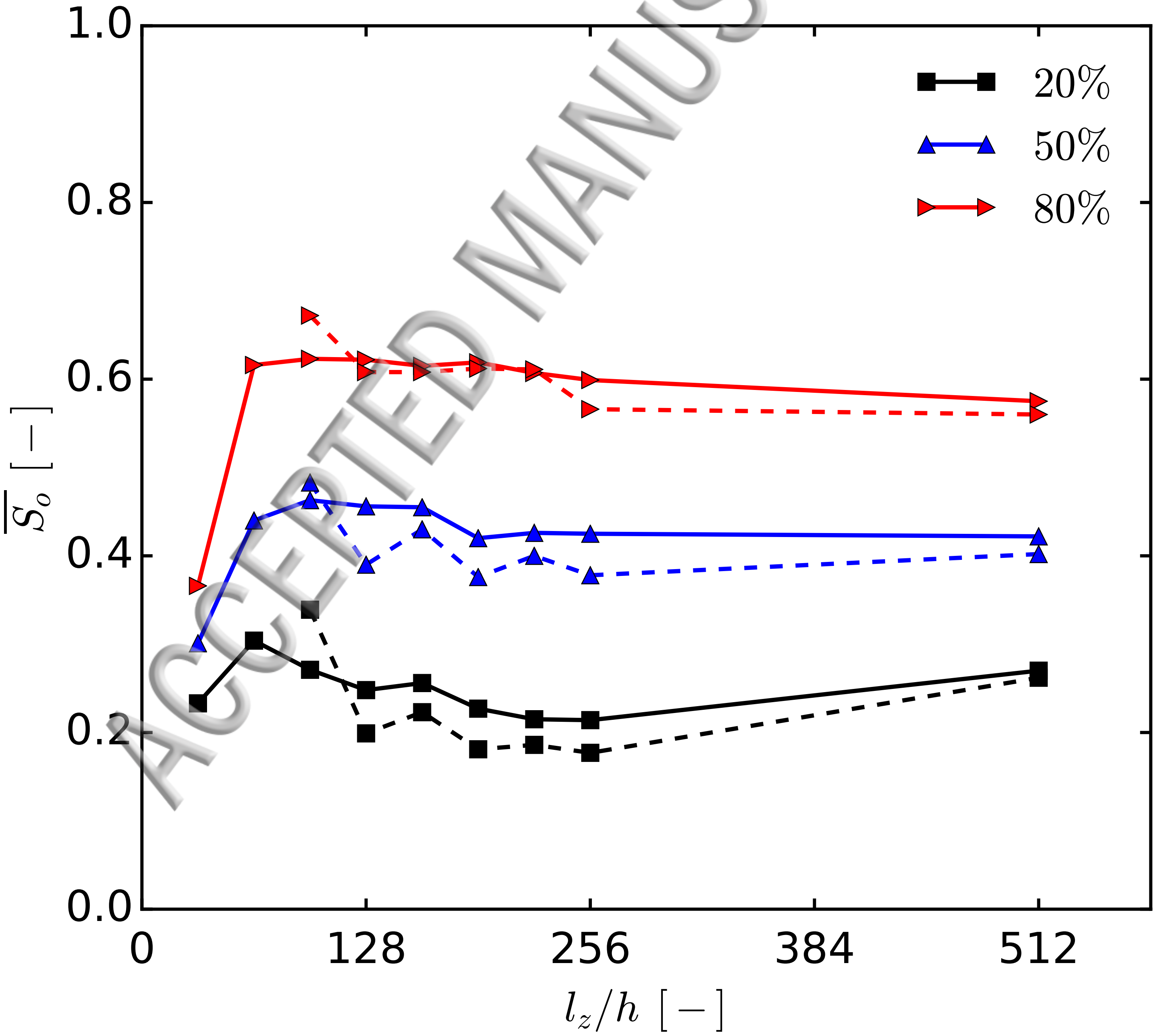
1.0
0.8
0.6
0.4
0.2
0.0
0
128
256
384
512
$\overline{S_o}$ $[-]$
l_z/h $[-]$
20%
50%
80%

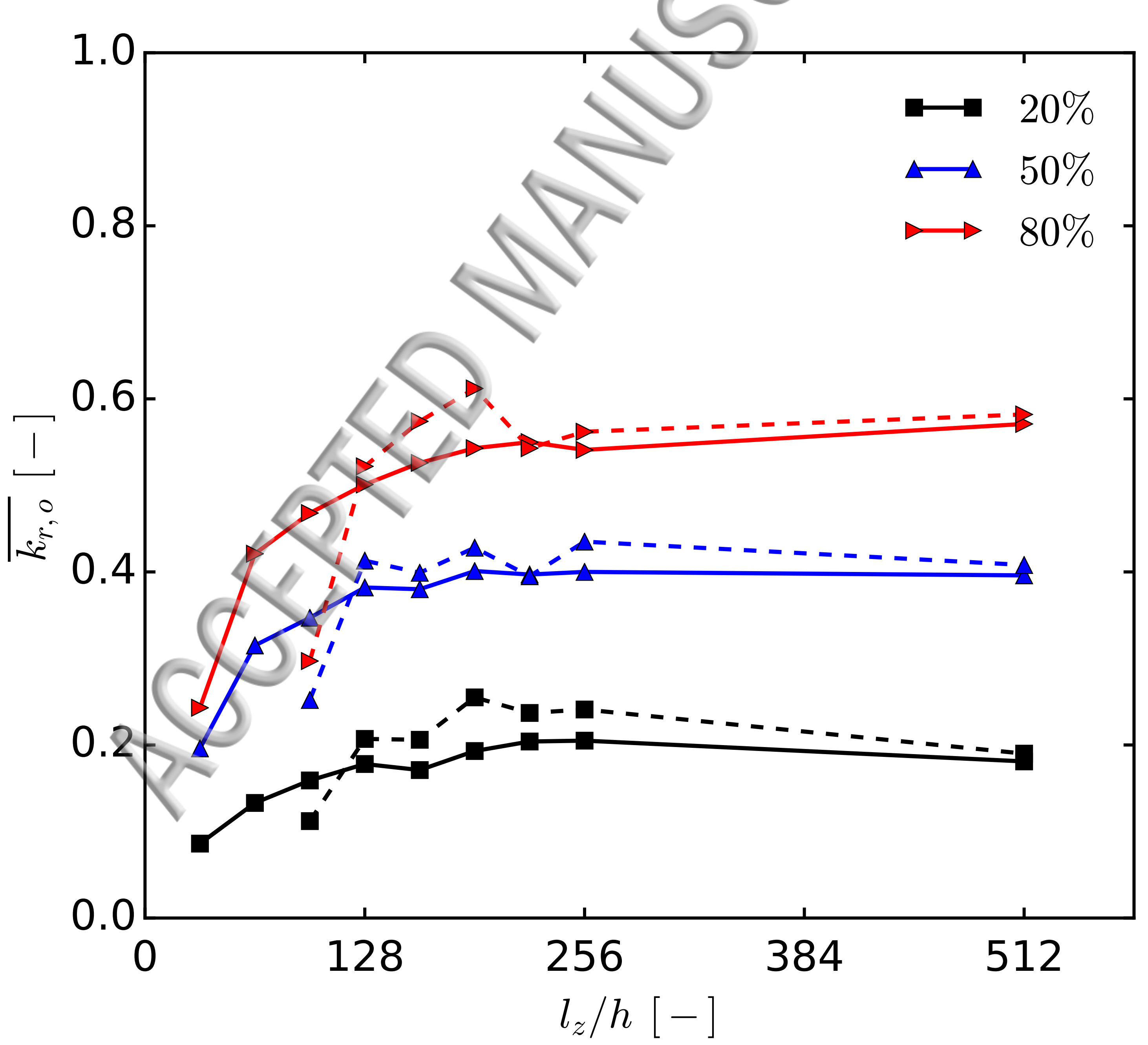
1.0
0.8
0.6
0.4
0.2
0.0
0
128
256
384
512
$\overline{k_{r,o}}$ $[-]$
l_z/h $[-]$
20%
50%
80%

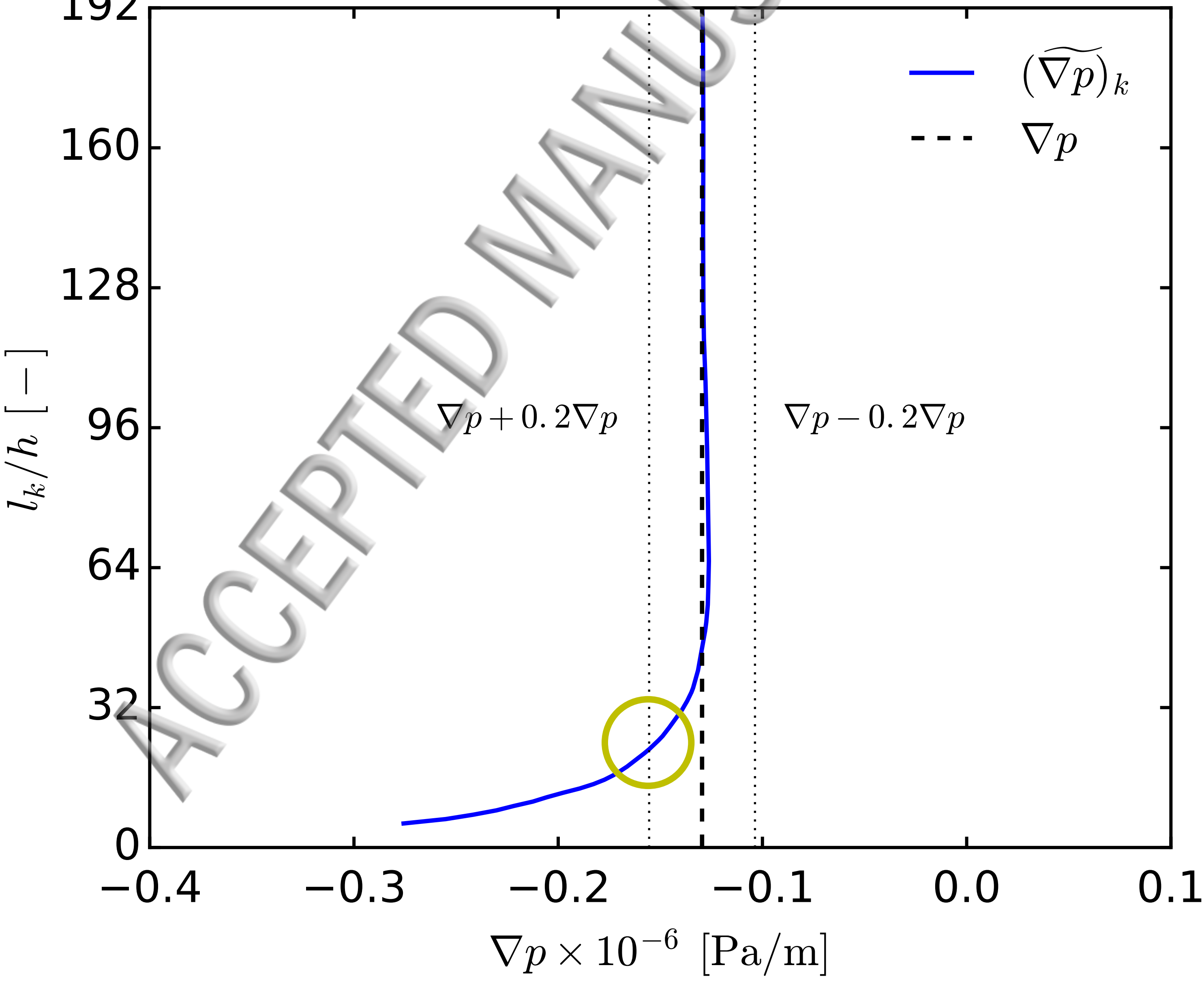
192
160
128
96
64
32
0
$l_k/h\ [-]$
−0.4
−0.3
−0.2
−0.1
0.0
0.1
$\nabla p \times 10^{-6}\ [\mathrm{Pa/m}]$
$(\widetilde{\nabla p})_k$
∇p
$\nabla p + 0.2\nabla p$
$\nabla p - 0.2\nabla p$

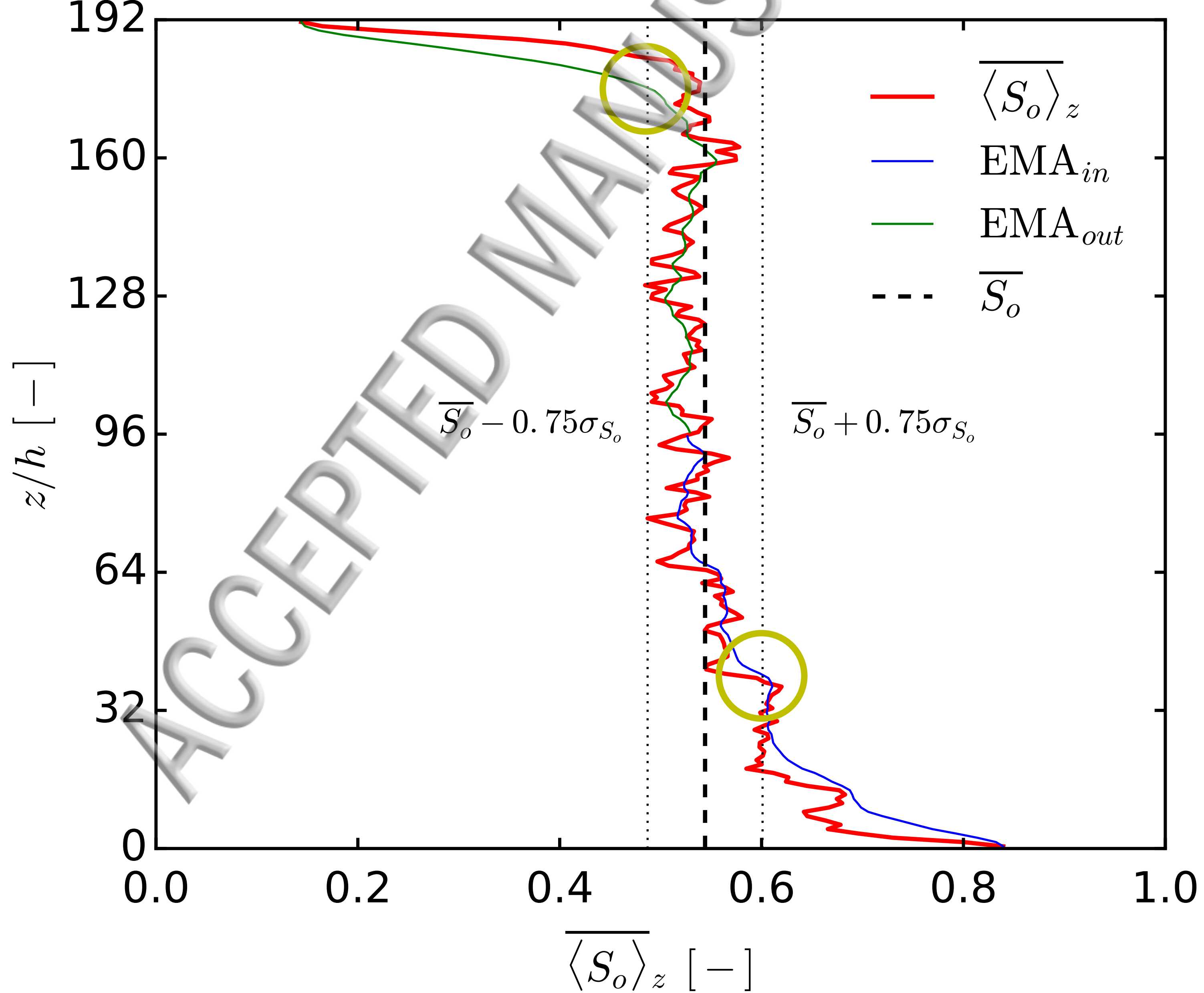

192
160
128
96
64
32
0
$z/h\ [-]$
0.0
0.2
0.4
0.6
0.8
1.0
$\overline{\langle S_o \rangle}_z\ [-]$
$\overline{\langle S_o \rangle}_z$
EMA_{in}
EMA_{out}
$\overline{S_o}$
$\overline{S_o} - 0.75\sigma_{S_o}$
$\overline{S_o} + 0.75\sigma_{S_o}$